NSEL Report Series
Report No. NSEL-028
August 2011

Model-Based Feedforward-Feedback Tracking Control for Real-Time Hybrid Simulation

Brian M. Phillips
and
Billie F. Spencer, Jr.

NSEL
NEWMARK STRUCTURAL ENGINEERING LABORATORY

Department of Civil and Environmental Engineering
University of Illinois at Urbana-Champaign

UILU-ENG-2011-1802

ISSN: 1940-9826

The Newmark Structural Engineering Laboratory (NSEL) of the Department of Civil and Environmental Engineering at the University of Illinois at Urbana-Champaign has a long history of excellence in research and education that has contributed greatly to the state-of-the-art in civil engineering. Completed in 1967 and extended in 1971, the structural testing area of the laboratory has a versatile strong-floor/wall and a three-story clear height that can be used to carry out a wide range of tests of building materials, models, and structural systems. The laboratory is named for Dr. Nathan M. Newmark, an internationally known educator and engineer, who was the Head of the Department of Civil Engineering at the University of Illinois [1956-73] and the Chair of the Digital Computing Laboratory [1947-57]. He developed simple, yet powerful and widely used, methods for analyzing complex structures and assemblages subjected to a variety of static, dynamic, blast, and earthquake loadings. Dr. Newmark received numerous honors and awards for his achievements, including the prestigious National Medal of Science awarded in 1968 by President Lyndon B. Johnson. He was also one of the founding members of the National Academy of Engineering.

Contact:
Prof. B.F. Spencer, Jr.
Director, Newmark Structural Engineering Laboratory
2213 NCEL, MC-250
205 North Mathews Ave.
Urbana, IL 61801
Telephone (217) 333-8630
E-mail: bfs@illinois.edu

The authors would like to acknowledge the support of the National Science Foundation under award CMMI-1011534, as well as Richard E. Christenson for the use of the 200 kN MR damper.

The cover photographs are used with permission. The Trans-Alaska Pipeline photograph was provided by Terra Galleria Photography (http://www.terragalleria.com/).

ABSTRACT

Substructure hybrid simulation is a powerful, cost-effective alternative for testing structural systems, closely coupling numerical simulation and experimental testing to obtain the complete response of a structure. In this approach, well-understood components of the structure are modeled numerically, while the components of interest are tested physically. Generally, an arbitrary amount of time may be used to calculate and apply displacements at each step of the hybrid simulation. However, when the rate-dependent behavior of the physical specimen is important, real-time hybrid simulation (RTHS) must be employed. Computation, communication, and servo-hydraulic actuator limitations cause delays and lags which lead to inaccuracies and potential instabilities in RTHS. This report proposes a new model-based servo-hydraulic tracking control method including feedforward-feedback links to achieve accurate tracking of the desired displacement in real-time. The efficacy of the proposed approach is demonstrated through RTHS of a nine-story steel building employing a 200 kN large-scale magnetorheological (MR) damper as the rate-dependent physical specimen.

CONTENTS

Chapter 1

INTRODUCTION

Earthquakes, strong winds, and tsunami are among the most destructive forces that civil infrastructure faces. Advances in supplemental energy dissipation devices, such as base isolation, fluid dampers, and friction devices, provide promising solutions for mitigating damage from these dynamic loads (Soong and Spencer, 2003). The responses of these devices are rate-dependent, requiring real-time experimental evaluation. When these devices are used as part of a hybrid simulation, real-time execution of the experiment is necessary to obtain accurate and stable results (i.e., real-time hybrid simulation (RTHS)).

Throughout a hybrid simulation, communication between the experimental and numerical components is maintained in a loop of action and reaction. For conventional hybrid simulation, delays in this loop are not critical, as the time-scale is greatly extended. On the other hand, delays/lags in RTHS can undermine the accuracy and stability of the experiment. Horiuchi et al. (1996) demonstrated that for a linear-elastic, single-degree-of-freedom (SDOF) system, the effect of the energy introduced by a time delay is equivalent to negative damping. This negative damping was shown to be large for experiments with large stiffness or a large time delay. If the negative damping exceeds the inherent structural damping in the system, the experiment will become unstable. Moreover, even if the system remains stable, the results may be inaccurate.

RTHS requires accurate tracking of the desired displacement using servo-hydraulic actuators. Close examination of the system response shows that experimental equipment introduces both a time delay and frequency-dependent time lag into the RTHS loop. Time delays are not a function of frequency, generally being caused by the communication of data, A/D and D/A conversion, and computation time. These delays can be reduced by using faster hardware, smaller numerical integration time steps, and more efficient software. In contrast, time lags are a result of the physical dynamics and limitations of the servo-hydraulic actuators and vary with both the frequency of excitation and specimen conditions (Dyke et al., 1995). Time delays and lags are an intrinsic part of experimental testing and mitigation of their effects is an essential part of RTHS.

A single apparent time delay, lumping together all of the actual time delays and lags present in the loop, is the basis for early efforts at real-time servo-hydraulic control for RTHS. For this reason, early approaches are referred to simply as delay compensation. Note that a pure time delay has a constant, unit gain; thus, these approaches also ignored the frequency dependent amplitude variation of the servo-hydraulic actuator response. One of the most widely used approaches for delay compensation is the polynomial extrapolation method (Horiuchi et al., 1996). In this approach, known displacements are fit in time with a polynomial, and the displacement after a constant time delay is extrapolated in time (predicted). The extrapolated displacement is then sent to the servo-controller as the commanded displacement. The accuracy and stability of this method become an issue when the time delay is large as compared to the smallest period of the structure. This constraint can be problematic for lightly-damped, stiff, or multi-degree-of-freedom (MDOF) structures. The polynomial extrapolation technique was improved by using a least-squares approach to fit the polynomial to any number of data points (Wallace et al., 2005). The benefit of this modification is that including more data points improves the extrapolation robustness to measurement noise. Another extrapolation

technique includes velocity and acceleration signals and uses an assumption of linearly varying acceleration when extrapolating the displacement after the apparent time delay (Horiuchi and Konno, 2001). Extrapolation techniques based on a single apparent time delay remain popular and will be used as a basis of comparison for the approach proposed herein.

Extrapolation methods have be improved by adding adaptive online estimation of the time delay. One of the first attempts to measure the time delay online was proposed by Darby et al. (2002). This research demonstrated that the apparent time delay depends on the stiffness of the physical specimen, which can change as the specimen undergoes damage. A best guess of the apparent time delay is used initially. Then, based on whether or not the measured signal is leading or lagging the desired signal, the delay estimate is updated. Ahmadizadeh et al. (2008) proposed an improvement to online delay estimation using the slopes of the desired and measured signals, demonstrating faster convergence and reduction in oscillations in the estimated delay. Although able to account for changes in specimen conditions and poor initial estimates for the time delay, these improvements still only provide ad hoc solutions to real-time servo-hydraulic control.

Because time lags are not constant, but rather frequency and specimen dependent, assuming a single time delay is not adequate to characterize the dynamic behavior of servo-hydraulic actuators. At the same time, extrapolation approaches have limited frequency bandwidth for accurate compensation, which diminishes as the apparent time delay increases. This problem is particularly acute when structural response is significant at multiple frequencies (e.g., MDOF structures). That is to say, an estimated apparent time delay may be appropriate for the first few natural frequencies, but may not provide accurate compensation at higher natural frequencies.

Recently, researchers have begun to address the servo-hydraulic system as a dynamic system, creating low-order transfer functions to represent the dynamics (Wallace et al., 2007; Chen and Ricles, 2010). Inverses of these models can provide accurate compensation over the frequency range for which the model is accurate. When MDOF structures are lightly damped in higher modes, there is a potential for instabilities to manifest due to unmodeled high frequency servo-hydraulic dynamics. A similar approach using a lead compensator to reduce phase lag was examined by Jung et al. (2007). These approaches are generally heuristic, designed to compensate for an observed time delay or time lag in the system.

Model-based servo-hydraulic control accounts directly for the frequency dependent dynamics (both amplitude and phase) of the servo-hydraulic system over a broad frequency range through accurate modeling. Carrion and Spencer (2007) and Carrion et al. (2009) formulated the real-time servo-hydraulic control problem as a feedforward-feedback tracking problem, creating a model-based feedforward controller and introducing simplified feedback control. The feedforward controller was implemented as a model inverse with a low-pass filter to create a proper inverse. This research also included a scheduling control method whereby a feedforward controller was developed for each of the two extremes of the expected specimen conditions. The transition between the two controllers was determined online using a bumpless transfer. The bumpless transfer method has merits for a specimen with behavior that is controlled by the user (e.g., the input current to magnetorheological (MR) dampers), however is not generally applicable (e.g., degrading structures). Also, the feedback controller employs a simple

proportional gain, but does not take advantage of the known dynamics of the system. Previous studies in model-based control focused on small-scale specimens. While these studies are valuable, large-scale specimens bring about a number of challenges for RTHS as well as real-time servo-hydraulic control.

This report proposes a systematic framework for model-based servo-hydraulic tracking control. The actuator tracking problem is reformulated as a regulator problem, and linear quadratic Gaussian (LQG) control theory applied. A new approach to develop the feedforward controller is presented that achieves excellent compensation over a broad frequency range. Additionally, a model-based feedback controller is designed to further improve tracking robustness and alleviate the need for online modification of the feedforward controller under changing specimen conditions. The efficacy of the model-based servo-hydraulic tracking control method proposed herein is demonstrated in the RTHS of a nine-story steel building employing a 200 kN large-scale MR damper as the physical specimen.

PROBLEM FORMULATION

Hybrid simulation, a fusion of experimental testing and numerical simulation, provides an efficient and cost-effective means by which to test large, complex structures. By employing substructing, this testing method saves the cost of constructing structural components for which the response is well understood and greatly reduces the required laboratory space and equipment. In this way, even small laboratories can create and conduct a broad range of structural tests. Because only the critical structural components are physically tested, they can be large or even full-scale representations of the actual component, reducing size effects. When testing a structural system with a new device or material for which numerical models are inadequate or simply do not exist, such components should be tested experimentally.

The equations of motion governing the structural response are solved using numerical integration with inputs from the numerically imposed force F^{N} (e.g., due to an earthquake) and measured restoring force R^{E} from the experimental component. In discrete time form, the equations of motion can be written as:

$$\mathrm{M}^{\mathrm{N}}\ddot{x}_{i+1} + \mathrm{C}^{\mathrm{N}}\dot{x}_{i+1} + R^{\mathrm{N}}_{i+1} + R^{\mathrm{E}}_{i+1}(x_{i+1}, \dot{x}_{i+1}, \ddot{x}_{i+1}) = F^{\mathrm{N}}_{i+1} \tag{2.1}$$

where M^{N} is the mass matrix of the numerical substructure, C^{N} is the linear damping matrix of the numerical substructure, R^{N} is the restoring force vector of the numerical substructure, R^{E} is the restoring force vector of the experimental substructure, F^{N} is the vector of excitation forces, and x_{i+1}, $\dot{x}_{i+1}$, and $\ddot{x}_{i+1}$ are vectors of displacement, velocity, and acceleration at time t_{i+1} (i.e., the $i^{th}+1$ time step). Note that the restoring force of the experimental substructure naturally includes contributions from static, damping, and inertial forces.

The central difference method is one of the most popular numerical integration schemes for RTHS (Nakashima et al., 1992; Darby et al., 1999; Horiuchi et al., 1999; Nakashima and Masaoka 1999; Horiuchi and Konno 2001; Wu et al., 2005). The central difference method is based on the following relationships between displacement, velocity and acceleration:

$$\dot{x}_i = \frac{x_{i+1} - x_{i-1}}{2\Delta t} \tag{2.2}$$

$$\ddot{x}_i = \frac{x_{i+1} - 2x_i + x_{i-1}}{\Delta t^2} \tag{2.3}$$

where Δt is the numerical integration time step. Equations (2.2) and (2.3) can be substituted into Equation (2.1) to create an explicit representation of the displacement for progressing the numerical integration (i.e., the future displacements are only based on current and previous displacements):

$$x_{i+1} = \left[\frac{1}{\Delta \mathrm{t}^2}\mathrm{M}^{\mathrm{N}} + \frac{1}{2\Delta \mathrm{t}}\mathrm{C}^{\mathrm{N}}\right]^{-1}\left[\frac{2}{\Delta \mathrm{t}^2}\mathrm{M}^{\mathrm{N}}x_i - \left(\frac{1}{\Delta \mathrm{t}^2}\mathrm{M}^{\mathrm{N}} - \frac{1}{2\Delta \mathrm{t}}\mathrm{C}^{\mathrm{N}}\right)x_{i-1} - R^{\mathrm{N}}_i - R^{\mathrm{E}}_i + F^{\mathrm{N}}_i\right] \tag{2.4}$$

The central difference method is chosen for its simplicity, although the proposed research can be employed readily with other numerical integration schemes.

Throughout a hybrid simulation, communication between the experimental and numerical substructures is maintained in a loop of action and reaction as presented in Figure 2.1. From numerical integration (i.e., Equation (2.4)), the displacements x for the experimental substructure are calculated and sent to the loading system. The loading system, typically comprised of servo-hydraulic actuators, generates the physical displacements x_{p} for the experimental substructure. The physical restoring force of the specimen R_{p} is measured using sensors and returned to the numerical substructure as R^{E} for the next step of numerical integration.

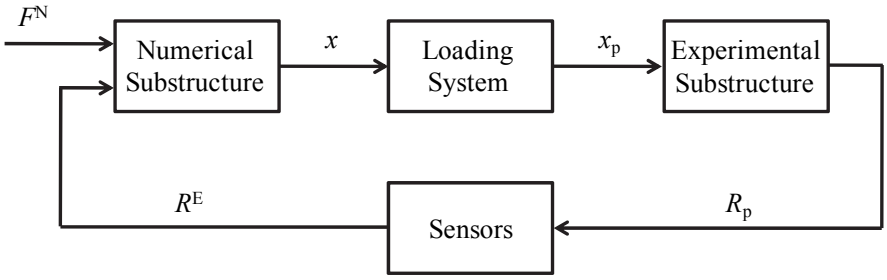

Figure 2.1: Schematic of a typical hybrid simulation.

In an ideal situation, the numerical substructure is directly coupled with the physical substructure, meaning that $x_{\mathrm{p}} = x$ (perfect displacement tracking) and $R^{\mathrm{E}} = R_{\mathrm{p}}$ (no delay/lag in the measurement of force). However, the loading system and sensors have their own inherent dynamics that are directly added into the dynamics of the closed-loop hybrid simulation. Rather than address the issue of time delay and time lag in a heuristic manner, control theory approaches will be used to develop accurate tracking control to directly address the sources of added (and unwanted) dynamics. Note that in RTHS, sensors typically do not use filters such that they do not introduce lag, thus focus will be placed on the loading system.

Consider the servo-hydraulic system, including the actuator, servo-valve, servo-controller, and specimen, as represented in Figure 2.2. This block diagram model from commanded displacement u to measured displacement y is proposed by Carrion and Spencer (2007) as a simplified, linearized model of the servo-hydraulic dynamics. The model includes the effects of control-structure interaction through natural velocity feedback, which directly couples the dynamics of the specimen and servo-hydraulic system (Dyke et al., 1995).

In this model, e_{c} is the error between commanded and measured displacements, K_{P} is the proportional feedback gain of the servo-controller, i_{c} is the command signal to the servo-valve, k_{v} is the valve gain, x_{v} is the valve spool displacement from the neutral position, Q_{L} is the oil flow through the load, K'_{q} is the valve flow gain, K'_{c} is the valve flow-pressure gain, p_{L} is pressure drop across the load, C_{l} is the total leakage coefficient of the actuator piston, V_{t} is the total volume of fluid under compression in both actuator chambers, β_{e} is the effective bulk modulus of the system, A is the area of the actuator piston, f_{p} is the force generated by the actuator piston, and b_0, b_1, and b_2 are parameters of the physical specimen.

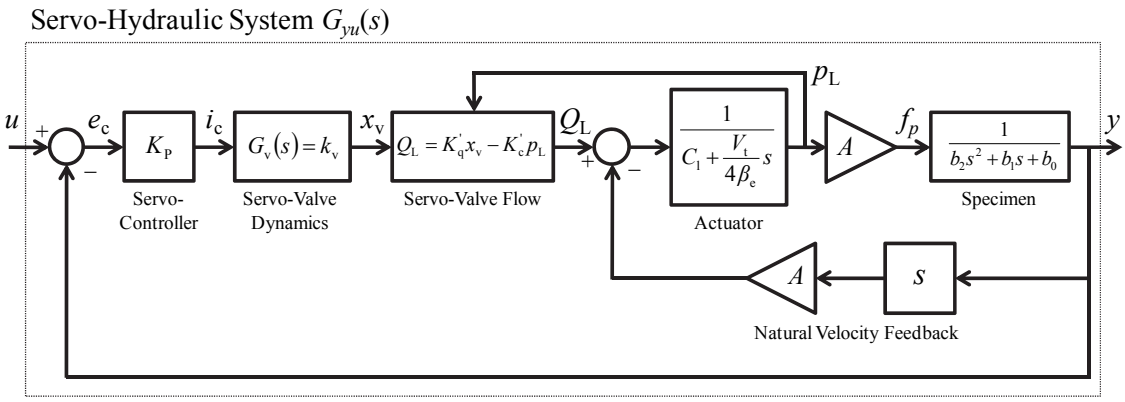

Figure 2.2: Block diagram model of the servo-hydraulic system.

The model can be represented by the following transfer function:

$$G_{yu}(s) = \frac{K_P \frac{K_q A}{K_c}}{\left(\frac{V_t}{4\beta_e K_c} b_2\right) s^3 + \left(b_2 + \frac{V_t}{4\beta_e K_c} b_1\right) s^2 + \left(b_1 + \frac{V_t}{4\beta_e K_c} + \frac{A^2}{K_c}\right) s + \left(b_0 + K_P \frac{K_q A}{K_c}\right)} \tag{2.5}$$

where $K_q = K_q' k_v$ is the servo-valve gain and $K_c = K_c' + C_l$ is the total flow pressure coefficient.

Equation (2.5) constitutes a three pole and no-zero transfer function of the linearized servo-hydraulic dynamics. Rather than identify each parameter, frequency domain system identification such as used in Chapter 4.2 can be used to simply identify the system poles and gain. Note that more detailed component models could be developed, resulting in higher order transfer functions. However, three pole models were found sufficient for this study and justified by Equation (2.5).

The proposed model-based servo-hydraulic tracking control approach employs feedforward and feedback control as an outer-loop controller around the servo-hydraulic system, such that the measured displacement y accurately tracks a desired displacement r (i.e., minimizing time delay, time lag, and amplitude errors). The proposed controller approach is illustrated in Figure 2.3.

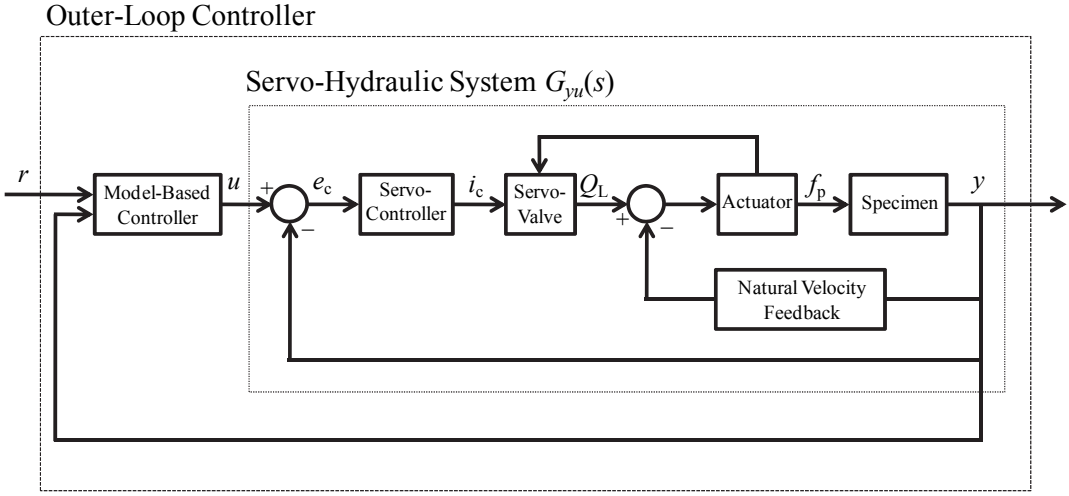

Figure 2.3: Block diagram of outer-loop controller.

The linearized dynamics of the servo-hydraulic system shown in Figures 2.2 and 2.3 can be represented by state space equations to facilitate modern control theory design:

$$\dot{z} = Az + Bu \tag{2.6}$$

$$y = Cz \tag{2.7}$$

where z is the state vector, $\dot{z}$ is the time derivative of the state vector, u is the system input, y is the measured system output and A, B, and C are the system, input, and output matrices, respectively.

The tracking error between the desired and measured displacement is defined by:

$$e = r - y \tag{2.8}$$

The command u to the actuator should be chosen such that the tracking error is minimized. If perfect tracking is achieved, an ideal state $\bar{z}$ and an ideal input $\bar{u}$ leading to an output $\bar{y}$ must exist such that $\bar{y} = r$. The ideal system is described as:

$$\dot{\bar{z}} = A\bar{z} + B\bar{u} \tag{2.9}$$

$$\bar{y} = C\bar{z} = r \tag{2.10}$$

Deviations of the state, control, and output from this ideal system with respect to the original system are defined as:

$$\tilde{z} = z - \bar{z} \tag{2.11}$$

$$\tilde{u} = u - \bar{u} \tag{2.12}$$

$$\tilde{y} = y - \bar{y} \tag{2.13}$$

The dynamics of the deviation system are then:

$$\dot{\tilde{z}} = A\tilde{z} + B\tilde{u} \tag{2.14}$$

$$\tilde{y} = C\tilde{z} = -e \tag{2.15}$$

The tracking problem has now been redefined as a regulator problem about a setpoint (Lewis and Syrmos, 1995). Equation (2.12) can be rearranged to represent the total control law in terms of the original system, which consists of a feedforward component $\bar{u} = u_{\mathrm{FF}}$ from the ideal system and a feedback component $\tilde{u} = u_{\mathrm{FB}}$ from the deviation system, i.e.,

$$u = \bar{u} + \tilde{u} = u_{\mathrm{FF}} + u_{\mathrm{FB}} \tag{2.16}$$

The next chapter describes how the feedforward and feedback controllers are designed.

DESIGN OF MODEL-BASED SERVO-HYDRAULIC TRACKING CONTROL

The model-based servo-hydraulic tracking controller, incorporating feedforward and feedback controllers, is represented schematically in Figure 3.1. In contrast to Figure 2.3, this figure shows the detail of the model-based controller block while condensing the servo-hydraulic system dynamics. The desired displacement r is modified by the feedforward controller and feedback controller to produce the commands u_{FF} and u_{FB}, respectively.

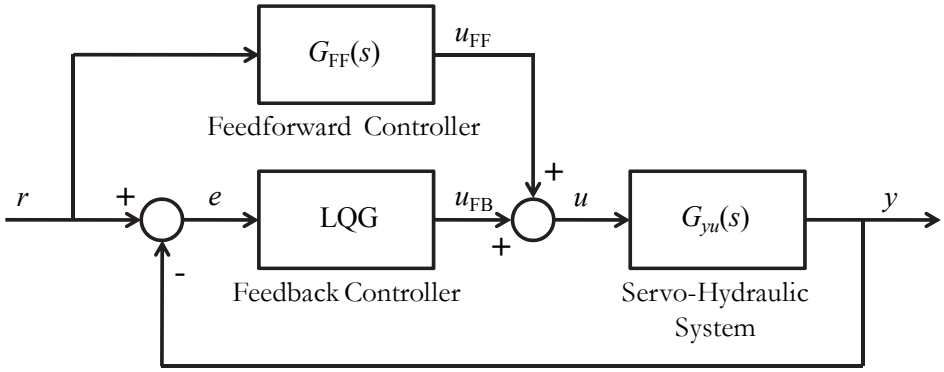

Figure 3.1: Block diagram of feedforward and feedback controller components.

3.1 Model-Based Feedforward Controller

To realize the feedforward controller, first a transfer function model of the servo-hydraulic system is identified from experimental data. The transfer function for the servo-hydraulic system can typically be represented as:

$$G_{yu}(s) = \frac{Y(s)}{U(s)} = \frac{K}{\prod_{i=1}^{N}(s-p_i)} \tag{3.1}$$

where N is the number of poles p_i and K is the gain of the model (Carrion and Spencer, 2007). Note that due to the phenomena of control-structure interaction, this transfer function will be dependent on the physical specimen to which the actuator is attached (Dyke et al., 1995).

The goal of the feedforward controller is to cancel the dynamics of the servo-hydraulic system using a model inverse. A pure inverse of Equation (3.1) would result in an improper transfer function as below.

$$G_{\mathrm{FF}}(s) = \frac{U(s)}{R(s)} = \frac{\prod_{i=1}^{N}(s-p_i)}{K} \tag{3.2}$$

The proposed approach to implement this improper model inverse is to make use of the displacement, velocity, acceleration, and higher order derivatives at the interface of the numerical and experimental substructures. Because the specimen should track this trajectory, the velocity, acceleration, and higher order derivatives can be used as long as

the signals are generated quickly and are not noisy. To avoid introducing noise from differentiating the displacement signal, the derivatives should be taken directly from the numerical integration if possible.

The following example demonstrates how to apply this approach to a three pole transfer function model combined with the central difference method for numerical integration. A three pole model in Equation (3.1) would result in an inverse that is improper by three degrees. In such a case, Equation (3.2) can be written as:

$$G_{\mathrm{FF}}(s) = \frac{U(s)}{R(s)} = a_0 + a_1 s + a_2 s^2 + a_3 s^3 \tag{3.3}$$

where the coefficients a_0 through a_3 are determined by expanding the expression in Equation (3.2) for $N = 3$. In the time domain, Equation (3.3) becomes:

$$u_{\mathrm{FF}}(t) = a_0 r(t) + a_1 \dot{r}(t) + a_2 \ddot{r}(t) + a_3 \dddot{r}(t) \tag{3.4}$$

where dots denote differentiation with respect to time. In general, the equations of motion are solved at the i^{th} time step and the $i^{th} + 1$ displacements are imposed on the physical specimen. In discrete time, Equation (3.4) can be written as:

$$u_{\mathrm{FF},i+1} = a_0 r_{i+1} + a_1 \dot{r}_{i+1} + a_2 \ddot{r}_{i+1} + a_3 \dddot{r}_{i+1} \tag{3.5}$$

The central difference method is explicit in displacement, thus only the desired displacement r_{i+1} is known, where $r_{i+1} = x_{i+1}$. The desired acceleration can be linearly extrapolated over one time step:

$$\ddot{r}_{i+1} = \ddot{x}_{i+1} = 2\ddot{x}_i - \ddot{x}_{i-1} \tag{3.6}$$

Note that the accelerations (and all other signals) must be in relative coordinates such that they describe the desired trajectory of the physical specimen. The desired velocity can be computed using Equation (3.7), which can be derived from Equations (2.2) and (2.3).

$$\dot{r}_{i+1} = \dot{x}_{i+1} = \dot{x}_i + \frac{\Delta t}{2}(\ddot{x}_i + \ddot{x}_{i+1}) \tag{3.7}$$

Finally, the desired jerk (derivative of the acceleration) can be calculated directly from the acceleration. Since a linear extrapolation of the acceleration is chosen, the jerk can be calculated as the slope of the extrapolation:

$$\dddot{r}_{i+1} = \dddot{x}_{i+1} = \frac{1}{\Delta t}(\ddot{x}_i - \ddot{x}_{i-1}) \tag{3.8}$$

The proposed feedfoward controller coupled with the central difference method is illustrated in Figure 3.2 as it would be implemented by a digital signal processor (DSP) for RTHS.

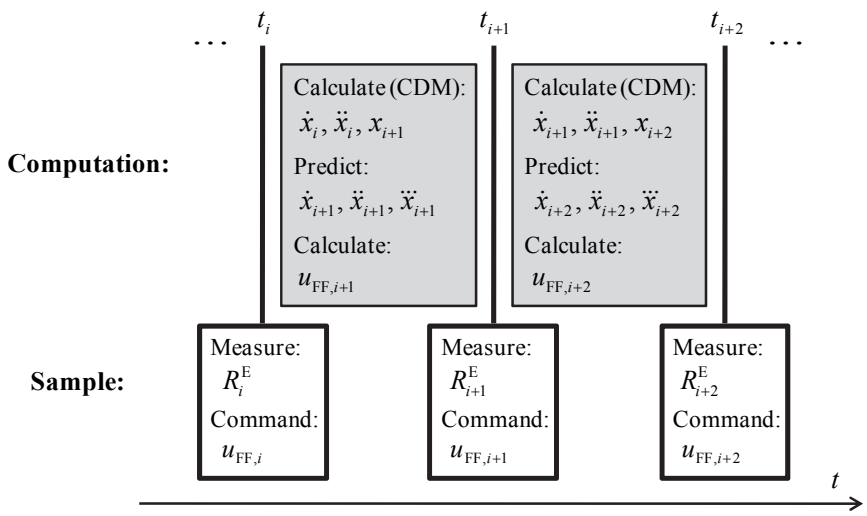

Figure 3.2: Implementation of proposed feedfoward controller in discrete time.

Depending on the numerical integration scheme and the degree to which the model inverse is improper, the above procedure may differ. Indeed there are many other alternatives to estimate higher order derivatives. Equations (3.6), (3.7), and (3.8) were found to produce the most accurate results among alternatives investigated. To illustrate the favorable performance, a sine wave displacement signal is considered. The velocity, acceleration, and jerk are calculated analytically by differentiating the sine wave. These signals are considered the exact solutions. Then, based on the information available at time t_i, the displacement, velocity, acceleration, and jerk are estimated for time t_{i+1}. Displacement is calculated using the central difference method equation:

$$x_{i+1} = x_i + \Delta t \dot{x}_i + \frac{\Delta t^2}{2} \ddot{x}_i \tag{3.9}$$

which can be derived from Equations (2.2) and (2.3). The accuracy of the displacement calculation can be seen as the accuracy of the central difference method itself.

Velocity, acceleration, and jerk are estimated using Equations (3.6), (3.7), and (3.8), respectively. The RMS error between the exact solutions and calculated/estimated values are then calculated over eight cycles of the sine wave. The exercise is repeated for multiple sine wave frequencies f_n ranging from 0.1 to 100 Hz and multiple sampling frequencies f_s from 500 Hz to 10,000 Hz where $f_s = 1/\Delta t$. The RMS errors are presented in Figure 3.2 in log-log scale with the frequency of the sine wave across the *x*-axis and each sampling frequency given its own data set. The accuracy of the calculations/estimations decreases with an increase in the frequency of the sine wave or a decrease in the sampling frequency. For a reasonable sampling frequency, such as 2000 Hz, the accuracy is excellent for displacement and velocity and acceptable for acceleration and jerk.

If higher order derivatives are not available or cannot be calculated accurately, a low-pass filter could be added to Equation (3.3) to reduce the degree to which the inverse is improper. Adding a sufficient number of poles, the low-pass filter can create a proper system, as in Carrion and Spencer (2007). However, low-pass filters typically introduce unwanted dynamics into the feedforward controller.

In some applications, the displacement signal is known a priori (e.g., earthquake motion reproduction); for such cases, smooth derivatives can be created offline using filters that do not introduce lag (e.g., weighted moving average) or smoothing splines.

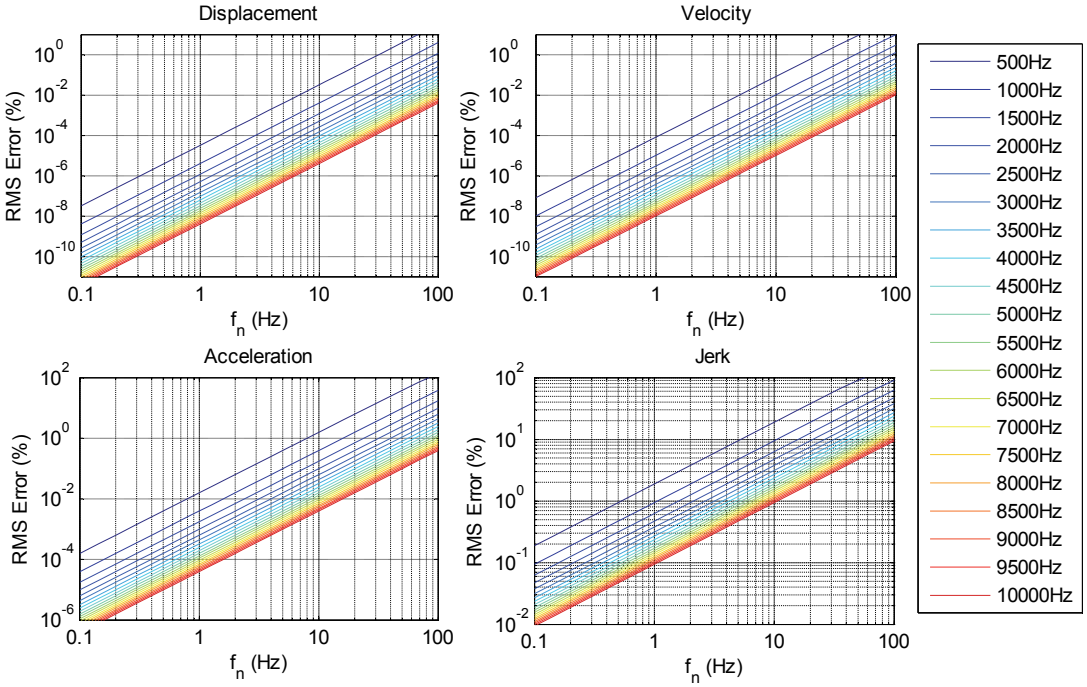

Figure 3.3: RMS Error between exact and estimated signals.

3.2 Model-Based Feedback Controller

In the presence of changing specimen conditions, modeling errors, and disturbances, LQG control can be applied to the deviation system to bring the deviation states to zero and thus reduce the tracking error. The deviation system is rewritten as:

$$\dot{\tilde{z}} = A\tilde{z} + Bu_{\mathrm{FB}} + Ew_{\mathrm{f}} \tag{3.10}$$

$$\tilde{y} = \mathrm{C}\tilde{z} + v_{\mathrm{f}} \tag{3.11}$$

where w_{f} is the disturbance to the system and v_{f} is the measurement noise. Only the output of the deviation system (i.e., $\tilde{y} = y - r$) is measurable. Thus, an observer is needed to estimate the unknown states of the deviation system. Evoking the separation principal, an LQG controller can be designed from independent LQR (optimal state feedback control) and Kalman filter (optimal observer) designs (Stengel, 1986).

To improve the LQG controller's tracking performance and robustness in the frequency range of interest, the disturbance w_{f} is assumed to be Gaussian white-noise w passed through a second-order shaping filter, i.e.,

$$\dot{z}_{\mathrm{f}} = A_{\mathrm{f}}z_{\mathrm{f}} + E_{\mathrm{f}}w \tag{3.12}$$

$$w_{\mathrm{f}} = C_{\mathrm{f}}z_{\mathrm{f}} \tag{3.13}$$

where

$$A_{\mathrm{f}} = \begin{bmatrix} 0 & 1 \\ -\omega_{\mathrm{f}}^2 & -2\xi_{\mathrm{f}}\omega_{\mathrm{f}} \end{bmatrix}, \quad E_{\mathrm{f}} = \begin{bmatrix} 0 \\ 1 \end{bmatrix}, \quad C_{\mathrm{f}} = [\omega_{\mathrm{f}}^2 \quad 2\xi_{\mathrm{f}}\omega_{\mathrm{f}}\eta_{\mathrm{f}}] \tag{3.14}$$

The parameters ξ_{f}, ω_{f}, and η_{f}, control the peak, bandwidth, and roll-off of the disturbance, respectively. The deviation system can be rewritten as an augmented system that includes the dynamics of the shaping filter. This augmented system, denoted by the subscript a, is given by:

$$z_{\mathrm{a}} = \begin{Bmatrix} z_{\mathrm{f}} \\ \tilde{z} \end{Bmatrix} \tag{3.15}$$

$$\dot{z}_{\mathrm{a}} = A_{\mathrm{a}} z_{\mathrm{a}} + B_{\mathrm{a}} u_{\mathrm{FB}} + E_{\mathrm{a}} w \tag{3.16}$$

$$\tilde{y} = C_{\mathrm{a}} z_{\mathrm{a}} + v_f \tag{3.17}$$

where

$$A_{\mathrm{a}} = \begin{bmatrix} A_{\mathrm{f}} & 0 \\ EC_{\mathrm{f}} & A \end{bmatrix}, \quad B_{\mathrm{a}} = \begin{bmatrix} 0 \\ B \end{bmatrix}, \quad E_{\mathrm{a}} = \begin{bmatrix} E_{\mathrm{f}} \\ 0 \end{bmatrix}, \quad C_{\mathrm{a}} = [0 \quad C] \tag{3.18}$$

and the measurement noise v_{f} is assumed to be a Gaussian white noise.

The control u_{FB} can be obtained using an LQR design assuming full state feedback as follows:

$$J_{\mathrm{LQR}} = \int_0^\infty \left[\tilde{y}^T Q_{\mathrm{LQR}} \tilde{y} + u_{\mathrm{FB}}^T R_{\mathrm{LQR}} u_{\mathrm{FB}}\right] dt \tag{3.19}$$

$$u_{\mathrm{FB}} = -K_{\mathrm{LQR}} z_{\mathrm{a}} \tag{3.20}$$

where K_{LQR} is the optimal state feedback gain matrix, J_{LQR} is the cost function minimized by LQR design, Q_{LQR} is the weighting matrix on the system outputs, and R_{LQR} is the weighting matrix on the system inputs.

The augmented system states z_{a} can be estimated using a Kalman filter:

$$\dot{\hat{z}}_{\mathrm{a}} = A\hat{z}_{\mathrm{a}} + Bu_{\mathrm{FB}} + L_{\mathrm{Kal}}(\tilde{y} - C\hat{z}_{\mathrm{a}}) \tag{3.21}$$

where $\hat{z}_{\mathrm{a}}$ represents the estimated states and L_{Kal} is the optimal observer gain matrix.

The control law in Equation (3.20) is then written in terms of the estimated states and included in the estimator.

$$u_{\mathrm{FB}} = -K_{\mathrm{LQR}} \hat{z}_{\mathrm{a}} \tag{3.22}$$

$$\dot{\hat{z}}_{\mathrm{a}} = \left(A - L_{\mathrm{Kal}} C - BK_{\mathrm{LQR}}\right)\hat{z}_{\mathrm{a}} + L_{\mathrm{Kal}} \tilde{y} \tag{3.23}$$

In this research, the LQG feedback controller is designed using the control systems toolbox in MATLAB.

EXPERIMENTAL SETUP AND CHARACTERIZATION

To demonstrate the efficacy of the proposed model-based servo-hydraulic tracking controller, a nine-story model building with MR dampers installed is investigated. Semi-active control devices such as MR dampers combine the desirable properties of both passive and active control devices. They have the ability to adapt to loading demands on the structure, as in an active control system; however, as with passive systems, they cannot inject energy into the system, eliminating stability concerns. Also, in the event of a power loss or controller damage, the devices function as passive energy dissipaters. With an MR damper, changes in the input current can be used to achieve forces predictably in advanced semi-active control algorithms (Spencer et al., 1997). By using RTHS as the experimental framework, the building can be modeled numerically while the MR dampers tested experimentally. Although the focus of this report is to verify model-based servo-hydraulic tracking control for RTHS, future studies will make use of this framework to investigate semi-active control algorithms and other MR damper implementation concerns.

The RTHS testing system at the University of Illinois is located in the Newmark Structural Engineering Laboratory (NSEL, http://nsel.cee.illinois.edu) and is a part of the Smart Structures Technology Laboratory (SSTL, http://sstl.cee.illinois.edu). The actuator, manufactured by the Shore Western Corporation, is rated at 556 kN (125 kips) with a stroke of ±152.4 mm (±6 in) and effective piston area of 271 cm^2 (42 in^2). A Schenck-Pegasus model 1800 three-stage servo-valve rated at 300 lpm (80 gpm) is employed. The model 1800 contains internal circuits to excite and demodulate the main-spool LVDT, making it appear as a two-stage servo-value to the servo-controller. Hydraulic oil is routed through a Schenck-Pegasus model 3170804S hydraulic service manifold, which is rated at 300 lpm (80 gpm). The displacement of the actuator is measured using an internal AC LVDT. A 445 kN (100 kip) Key Transducers, Inc. model 1411-114-02 load cell in line with the actuator measures the restoring force of the attached specimen. The actuator and specimen (MR damper) are both mounted on a 7.62 cm (3 in) thick steel plate. Steel blocks and wedges are used to prevent differential movement of the actuator and specimen. The steel plate is secured to the NSEL strong floor using threaded rods to prevent flexing of the plate, and shear keys are used to prevent longitudinal translation of the plate. The frame is designed to minimize backlash and elastic deformation under the high forces produced during testing. This setup (see Figure 4.1) has proven successful for the dynamic testing of large-scale MR dampers (Yang et al., 2002; Phillips et al., 2010). In addition, the temperature is monitored continuously during testing using three Omega Engineering model SA1XL-J thermocouples and model SMCJ-J analog converters.

A Shore Western model 1104 digital servo-controller is used to control the actuator in displacement feedback mode. The servo-controller accepts externally generated commands from a dSPACE model 1103 DSP board. The DSP board is mounted in an external chassis and connected to a host computer via fiber optic cable. This board is used to perform numerical integration of the equations of motion for the numerical substructure, apply the real-time servo-hydraulic control, and compute the desired current for the MR damper based on specified semi-active control algorithms. These three numerical components are programmed on the host computer using Simulink, a block

diagram style programming tool within MATLAB. The Simulink model is converted to C language using MATLAB's Real-Time Workshop and transferred to the DSP board. Real-time execution of the code is controlled and monitored from the host computer. The host computer also acts as the DAQ, logging data from specified channels within the Simulink model. Numerical integration is performed using the central difference method with a sampling rate of 2000 Hz.

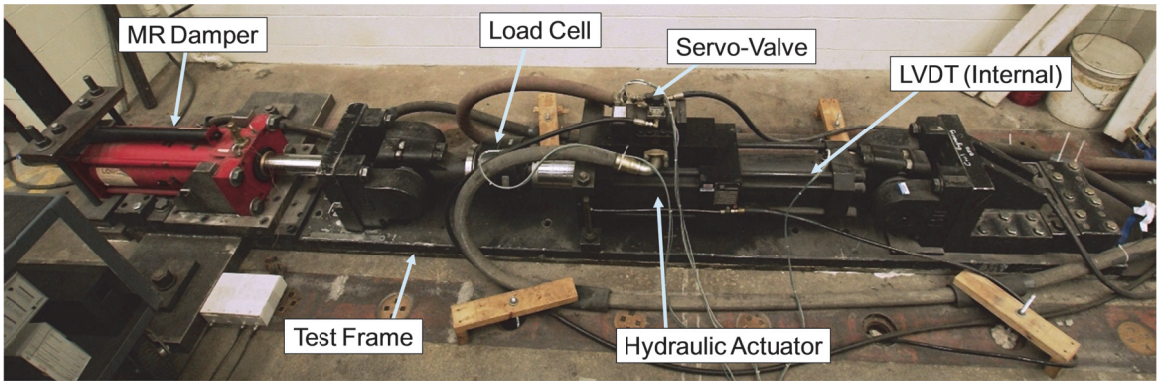

Figure 4.1: Test frame at the University of Illinois.

4.1 MR Damper Specimen

The test specimen used in this paper is a second-generation, large-scale 200 kN MR damper manufactured by the Lord Corporation. The damper has a stroke of ±292 mm (±13 in) and can generate forces slightly higher than the nominal 200 kN. The damper has an accumulator charged to 5.17 MPa (750 psi) to compensate for the thermal expansion of the MR fluid (Christenson et al., 2008).

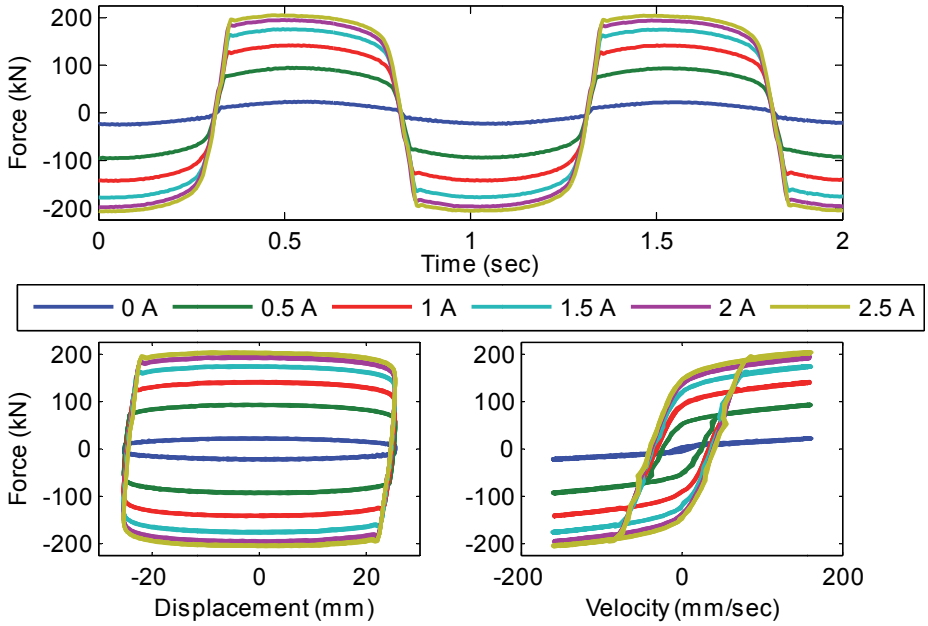

Figure 4.2: MR damper response to a 25.4 mm, 1 Hz sine wave at select levels of current.

The current to the MR damper is controlled using a pulse-width modulator, which consists of an Advanced Motion Controls model PS2x300W unregulated power supply providing 80 VDC to an Advanced Motion Controls model 20a8 analog servo-drive. The analog servo-drive can measure the current in the closed-loop circuit and use this signal for current feedback control, which is suitable for MR damper applications. The benefit of using a pulse-width modulator is power efficiency and quick response time.

The MR damper responds to increases in current with corresponding increases in the restoring force during dynamic events. The responses of the damper to a 25.4 mm, 1 Hz sine wave at six different levels of input current are presented in Figure 4.2. As can be seen, the response is velocity dependent and highly nonlinear. At the same time, the magnitude of the restoring force changes dramatically, yet predictably with the input current. This characteristic makes MR dampers ideal for semi-active structural control.

4.2 Characterization of the Servo-Hydraulic System

The transfer function from the input commanded displacement to the output measured displacement $G_{yu}(s)$ of the servo-hydraulic system was calculated over a wide range of frequencies. This transfer function includes the dynamics of the actuator, servo-valve, servo-controller, and specimen. Note that some time delay (e.g. data communication, A/D and D/A conversion) will naturally be included in a characterization of the servo-hydraulic system dynamics. The input was selected as a band-limited white noise (BLWN) from 0 to 50 Hz with a displacement RMS of 0.254 mm, providing insight into the servo-hydraulic dynamics over this range of frequencies. The dSPACE system was used to generate the commanded signal and measure the response at 16,384 Hz to avoid aliasing. Data was down-sampled to 128 Hz and the transfer function was calculated using 2048 FFT points, a Hanning window with 50% overlap, and 10 averages.

Because the current to the MR damper can change during the RTHS, the servo-hydraulic dynamics must be investigated at multiple current levels. The measured transfer function magnitude, phase, and time lag are presented in Figure 4.3 for two conditions: 0.0 and 2.5 Amps. The results are also averaged to create a third transfer function at average conditions. Time lag is calculated by dividing the phase by the frequency, which is sensitive to noise at the lower frequencies. Transfer function models are overlain on Figure 4.3 in dashed black lines. Three pole models are found sufficient to accurately represent the dynamics over the frequency range of interest (up to 40 Hz). Models of the servo-hydraulic dynamics at 0.0 and 2.5 Amps, as well as an average of the two specimen conditions, are given by:

$$G_{yu,0.0A}(s) = \frac{1.730\times10^{7}}{(s+182.7)(s^{2}+225.3s+9.499\times10^{4})} \tag{4.1}$$

$$G_{yu,2.5A}(s) = \frac{1.613\times10^{7}}{(s+134.2)(s^{2}+324.6s+1.211\times10^{5})} \tag{4.2}$$

$$G_{yu,\mathrm{avg}}(s) = \frac{1.600\times10^{7}}{(s+151.7)(s^{2}+250.4s+1.061\times10^{5})} \tag{4.3}$$

Figure 4.3 shows that the behavior of the servo-hydraulic system is frequency dependent, where the magnitude and phase (or equivalently, the time lag) vary with frequency. Typical time lags reported in the literature range from 8 to 30 msec (Horiuchi et al., 1999; Nakashima and Masaoka, 1999; Darby et al., 2001; Darby et al., 2002; Shing et al., 2004; Wallace et al., 2007; Ahmadizadeh et al., 2008; Chen and Ricles, 2010). The time lag in this experimental setup was found to vary between 8 and 11 msec depending on the frequency of excitation and the specimen conditions, which is relatively small for such a large actuator. Subsequent tests comparing the lag between input sine waves and measured responses confirmed these results. Traditional delay compensation approaches based on a single constant time delay would be inadequate for systems that respond at multiple frequencies, such as MDOF structures. Likewise, traditional approaches do not address the decay in magnitude observed.

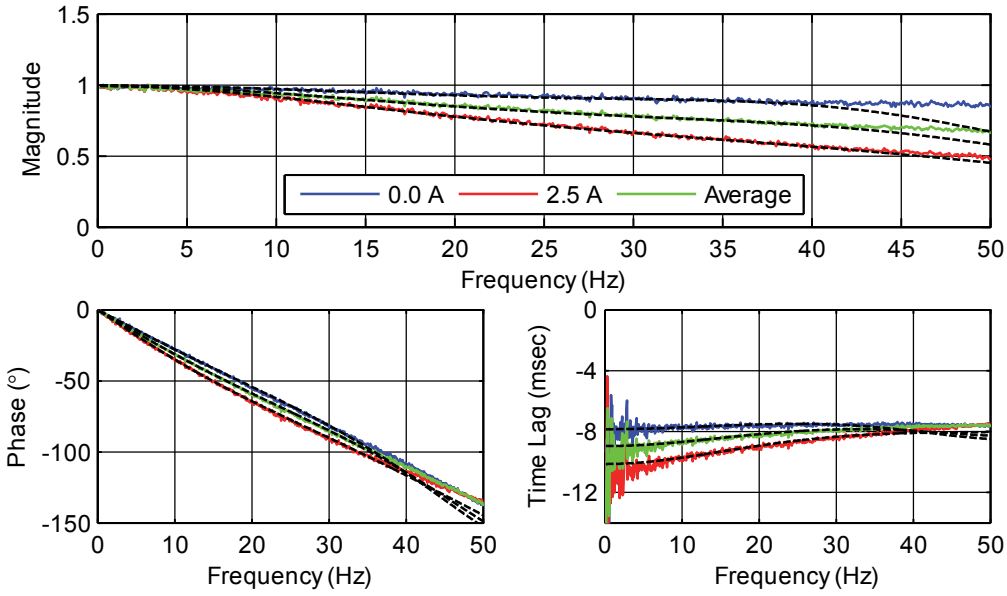

Figure 4.3: Measured system transfer functions $G_{yu}(s)$ at select current levels (dashed lines represent fitted transfer function models).

EXPERIMENTAL EVALUATION OF FEEDFORWARD-FEEDBACK DESIGN

Based on the methods proposed in Chapter 3.1, three model-based feedforward controllers are created using the transfer function models in Equations (4.1), (4.2), and (4.3) and identified as $G_{\mathrm{FF,0.0A}}(s)$, $G_{\mathrm{FF,2.5A}}(s)$, and $G_{\mathrm{FF,avgA}}(s)$, respectively. To improve performance and compensate for system modeling errors and changes in specimen conditions, a model-based LQG feedback controller is created using the transfer function model in Equation (4.3) along with the method proposed in Chapter 3.2.

As a comparison with the previous model-based approach (Carrion and Spencer 2007), two feedforward controllers are created based on the transfer function models in Equations (4.1) and (4.2) with the low-pass filters and identified as $G_{\mathrm{FF,0.0A}}(s)$ + LP and $G_{\mathrm{FF,2.5A}}(s)$ + LP. For cases when the specimen conditions may be changing, a bumpless transfer is created between the two feedforward controllers based on the input current $0.0 \leq i_{\mathrm{d}} \leq 2.5$ Amps.

To provide further comparison, three 3rd order polynomial extrapolation compensators are created, based on 8 msec delay for 0.0 Amps, 10 msec delay for 2.5 Amps, and 9 msec delay for changing specimen conditions. Also, three single pole single zero lead compensator designs are created, one to provide good compensation at 0.0 Amps, one to provide good compensation at 2.5 Amps, and one to provide good compensation under average specimen conditions.

All real-time servo-hydraulic controllers above are created assuming a 2000 Hz sampling frequency. Table 5.1 summarizes the controllers explored.

Table 5.1: Real-time servo-hydraulic controllers.

Method	*Specimen Conditions*	*Short Name*
Proposed Model-Based Tracking Control	0.0 Amps	$G_{\mathrm{FF,0.0A}}(s)$
	0.0 Amps	$G_{\mathrm{FF,0.0A}}(s)$ + LQG
	2.5 Amps	$G_{\mathrm{FF,2.5A}}(s)$
	Average / General	$G_{\mathrm{FF,avgA}}(s)$ + LQG
Model-Based Control with Low-Pass Filter	0.0 Amps	$G_{\mathrm{FF,0.0A}}(s)$ + LP
	2.5 Amps	$G_{\mathrm{FF,2.5A}}(s)$ + LP
	Average / General	Bumpless + LP
3rd Order Polynomial Extrapolation	0.0 Amps	3rd Poly 8ms
	2.5 Amps	3rd Poly 10ms
	Average / General	3rd Poly 9ms
Lead Compensator (Single Pole, Single Zero)	0.0 Amps	Lead Comp 8ms
	2.5 Amps	Lead Comp 10ms
	Average / General	Lead Comp 9ms

5.1 Tracking Performance in the Frequency Domain

To evaluate the performances in the frequency domain, the real-time servo-hydraulic controllers were implemented in dSPACE. Then, a BLWN from 0−50 Hz with a displacement RMS of 0.254 mm was commanded to experimentally determine the compensated servo-hydraulic system transfer function $G_{yr}(s)$ (see Figure 2.3). Controllers were designed to match the specimen conditions, with results for the 0.0 Amp condition in Figure 5.1 and the 2.5 Amp condition in Figure 5.2. Perfect controller performance would be indicated by unity magnitude, zero phase, and zero time lag over the frequency range of interest.

The polynomial extrapolation technique provides good compensation at low-frequencies. However, magnitude undershoot is found from 5 to 15 Hz, whereas above 15 Hz the magnitude begins to increase dramatically. Because of this amplification, the system was not excited above 30 Hz for safety. At the same time, the polynomial extrapolation technique overcompensates for the time lag after 10 Hz. This overcompensation can add positive damping to the RTHS loop, adding stability while compromising accuracy. After about 25 Hz, the polynomial extrapolation technique begins to undercompensate. Although this study was only performed up to 30 Hz, using analytically derived transfer functions the trend of under-compensation is known to continue past 30 Hz.

The lead compensator also provides good compensation at low-frequencies. However, at about 10 Hz, the magnitude begins to increase significantly and the time lag becomes undercompensated. A single pole and zero pair are not enough to provide adequate compensation over a broad frequency range, which can be problematic if high-frequency response is expected.

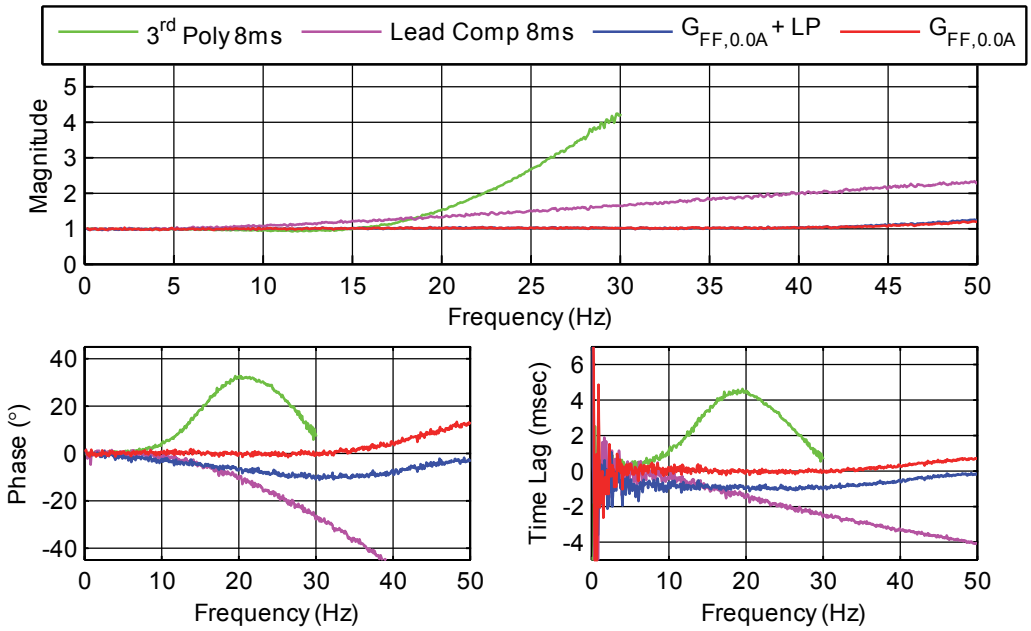

Figure 5.1: Transfer functions $G_{yr}(s)$ for various control techniques with 0.0 Amps in damper.

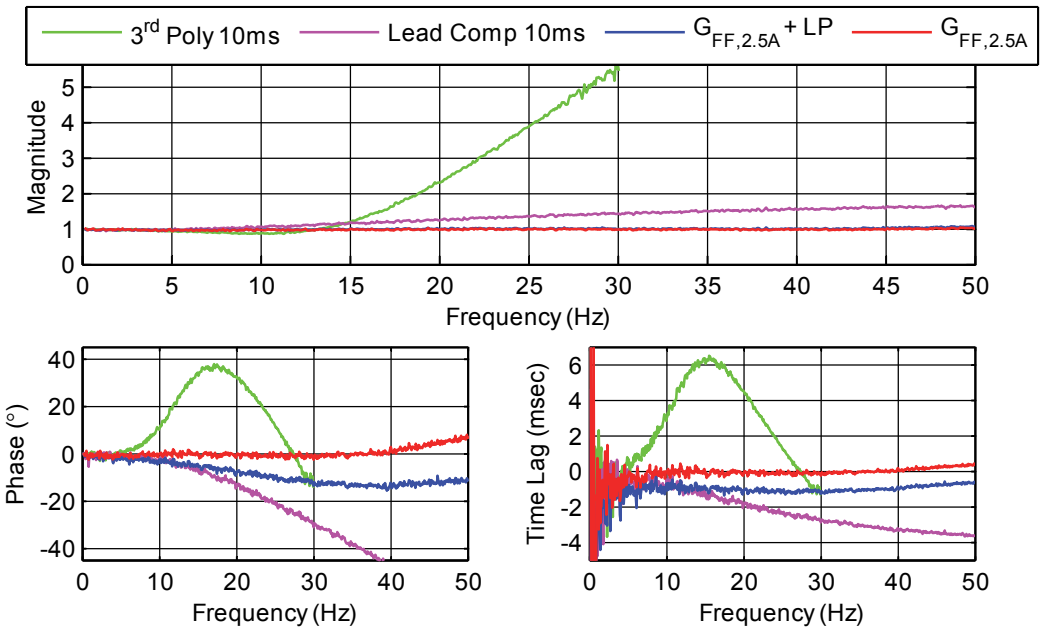

Figure 5.2: Transfer functions $G_{yr}(s)$ for various control techniques with 2.5 Amps in damper.

These results demonstrate the model-based approaches to have significantly better performance in terms of both magnitude and phase (or time lag). Excellent results can be seen in magnitude performance for model-based approaches up to 50 Hz. In terms of phase, the model-based approach using a low-pass filter has slightly poorer time lag compensation, which is due to the dynamics of the low-pass filter adversely adding phase lag to the model-based inverse.

5.2 Tracking Performance in the Time Domain

Real-time servo-hydraulic control using the above controllers was evaluated in the time domain using a predefined displacement and current command history. Two displacement histories were explored (a) BLWN with bandwidth of 0−5 Hz and an RMS of 2.78 mm and (b) BLWN with bandwidth of 0−15 Hz and an RMS of 0.595 mm. During this displacement, the current command to the MR damper was either maintained at 0.0 Amps (passive-off), 2.5 Amps (passive-on), or a pulse between 0.0 Amps and 2.5 Amps at 0.5 Hz (50% duty cycle, mimicking semi-active control conditions). Results of the time domain tracking tests are presented in Table 5.2. Good tracking is indicated by a low RMS error between the desired and measured displacements.

Results highlight that the proposed model-based servo-hydraulic tracking control technique provides considerable improvement in system performance through reduction of the RMS error for all specimen conditions. Model-based feedforward controllers designed to match the specimen conditions performed well while the general model-based feedforward-feedback controller performed well under all specimen conditions.

Table 5.2: Tracking performance for predefined displacement histories.

Current Command	*Controller*	*RMS Error (%) 0−5 Hz BLWN*	*RMS Error (%) 0−15 Hz BLWN*
0.0 Amps	None	16.0	42.9
	3rd Poly 8ms	1.22	12.8
	Lead Comp 8ms	1.95	13.3
	$G_{\mathrm{FF,0.0A}}(s)$ + LP	1.01	4.27
	$G_{\mathrm{FF,0.0A}}(s)$	0.942	3.45
	$G_{\mathrm{FF,avgA}}(s)$ + LQG	1.16	3.89
2.5 Amps	None	20.1	51.7
	3rd Poly 10ms	2.04	25.9
	Lead Comp 10ms	3.34	15.1
	$G_{\mathrm{FF,2.5A}}(s)$ + LP	2.55	9.40
	$G_{\mathrm{FF,2.5A}}(s)$	2.27	4.68
	$G_{\mathrm{FF,avgA}}(s)$ + LQG	1.14	5.57
2.5 Amp Pulse	None	18.1	49.2
	3rd Poly 9ms	1.80	18.3
	Lead Comp 9ms	2.97	16.0
	Bumpless + LP	2.04	8.45
	$G_{\mathrm{FF,avgA}}(s)$	1.93	6.35
	$G_{\mathrm{FF,avgA}}(s)$ + LQG	1.09	4.72

Figure 5.3 shows the time history results for the displacement tracking experiment corresponding to the 2.5 Amp pulse. The measurements have been fit with a spline curve to reduce noise for ease of observation. Both 0−5 Hz BLWN and 0−15 Hz BLWN results are presented at 3 seconds with identical scaling in both displacement and time. At 3 seconds, the current is switched from 0.0 Amps to 2.5 Amps, thus the results show a transition period in specimen conditions. Without compensation, the effect of the servo-hydraulic dynamics on magnitude and phase are apparent.

The time history results reflect the observations made in the frequency domain study. The 3rd order polynomial extrapolation approach shows slight undershoot at these frequencies. At the same time, the time lag is overcompensated, especially in the 0−15 Hz BLWN case. The lead compensator exhibits considerable overshoot, especially in the 0−15 Hz BLWN case. The time lag is slightly overcompensated in the 0−5 BLWN Hz case before 3 seconds because the lead compensator is designed for average conditions and the specimen is at 0.0 Amps. In the 0−15 Hz BLWN case, the time lag is undercompensated because the effectiveness of the lead compensator diminishes at high-frequencies. With the bumpless transfer approach, the time lag is well compensated under changing specimen conditions however there is a slight overshoot in magnitude. With the proposed model-based feedforward-feedback controller, accurate tracking of both magnitude and phase is achieved.

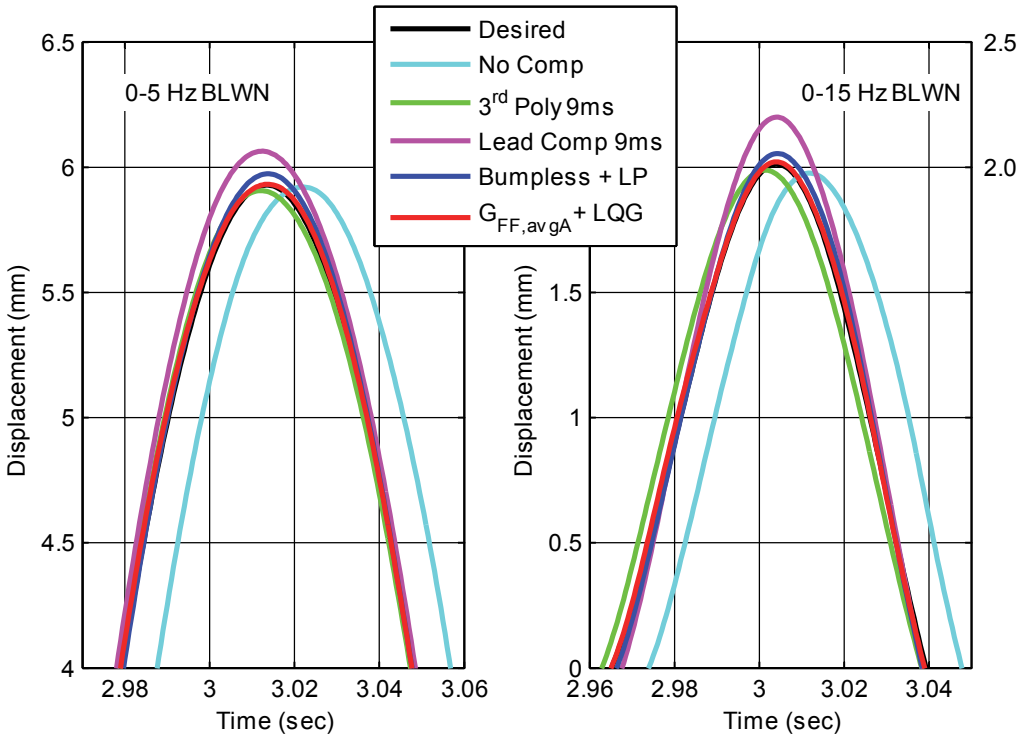

Figure 5.3: Displacement tracking during a pulse in current.

5.3 Preliminary Real-Time Hybrid Simulation Study

To illustrate the real-time servo-hydraulic controller performances in a closed-loop RTHS, a simple SDOF structure is selected. Mass, damping, and stiffness are simulated numerically while an MR damper at 0.0 Amps is used as the physical substructure. At this level of current, the MR damper can obtain approximately 20 kN restoring force, which would provide an appropriate level of control (approximately 10% of the mass) for a 20,000 kg structure. With the mass held constant, the stiffness is varied to achieve a set of structures with natural frequencies ranging from 0.5 Hz to 30 Hz. Although it is not likely that a civil engineering structure will have a single mode at such high frequencies, MDOF structures may possess modes in this range or beyond. For each structure, the damping coefficient is chosen to achieve 2% damping.

Each structure is excited with a BLWN ground acceleration from 0−30 Hz. The RMS values of the ground acceleration were chosen as 1000 mm/s^2 for the 0.5 and 1 Hz structures, 1500 mm/s^2 for the 5 Hz structure, and 2000 mm/s^2 for the 10, 20, and 30 Hz structures. These RMS values were chosen to provide a safe level of excitation while achieving a response significantly above the noise floor of the measurement devices. Each structure was tested using no compensation, the 3rd order polynomial extrapolation, lead compensator, model-based feedforward control with a low-pass filter, and the proposed model-based feedforward control with and without feedback. Results are presented in Figure 5.4 with each experiment summarized by the RMS error between the desired and measured displacement.

All real-time servo-hydraulic control schemes provide improved tracking when compared to the uncompensated case, except for the 3rd order polynomial extrapolation for the 30 Hz structure. In this case, the response became amplified so greatly that the experiment was unsafe to continue. The 3rd order polynomial extrapolation and lead compensators are not accurate in magnitude or phase at higher frequencies, leading to poor performance in RTHS. The model-based feedforward controller with a low-pass filter works well, however the added filter dynamics detract from controller performance at high frequencies. The proposed model-based feedfoward controller exhibits the best results over a wide range of frequencies. Thus, if a structure exhibits higher frequency responses, the proposed method would be able to provide the best tracking and avoid instability. Adding model-based feedback control further improves performance over the lower frequency region (as was desired for this particular feedback controller design).

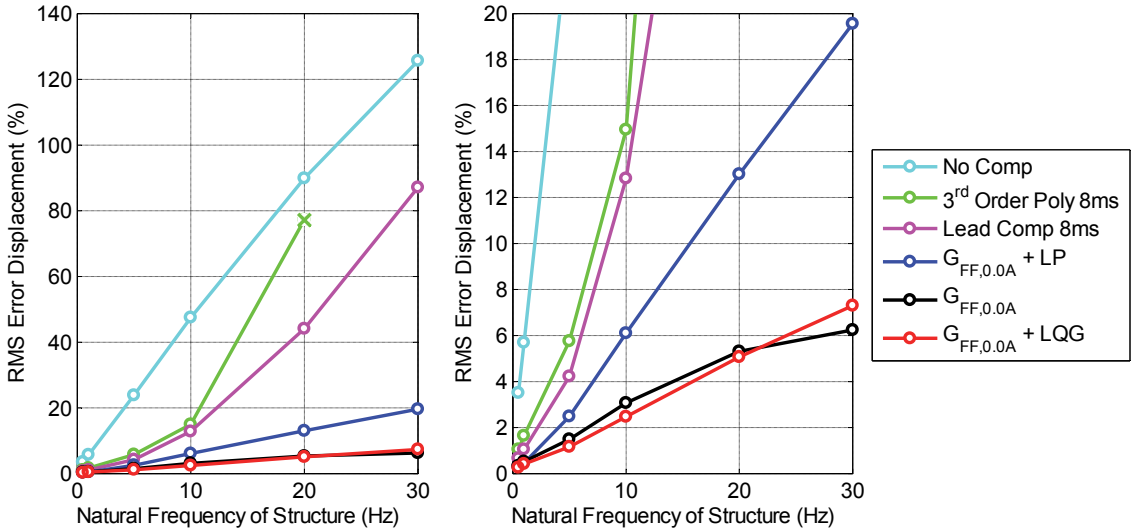

Figure 5.4: RMS error for RTHS of SDOF structure.

REAL-TIME HYBRID SIMULATION OF A SEMI-ACTIVELY CONTROLLED STRUCTURE

To verify the model-based servo-hydraulic tracking control technique for large-scale real-time hybrid testing, a well-researched nine-story steel frame benchmark shear building is chosen (Ohtori et al., 1994). This structure was designed to meet seismic code and represent a typical medium-rise building in Los Angeles, California. This structure has five bays in both the NS and EW directions. The NS lateral load system consists of two identical moment resisting frames as shown in Figure 6.1. For this research, a linear model of one of these NS moment resisting frames is used with half of the total seismic mass of the structure and excited in the NS direction.

The natural frequencies of the structure corresponding to the first five modes are 0.443, 1.18, 2.05, 3.09, and 4.27 Hz, respectively, with a maximum natural frequency of 63.6 Hz. All modes are assumed to have 2% damping.

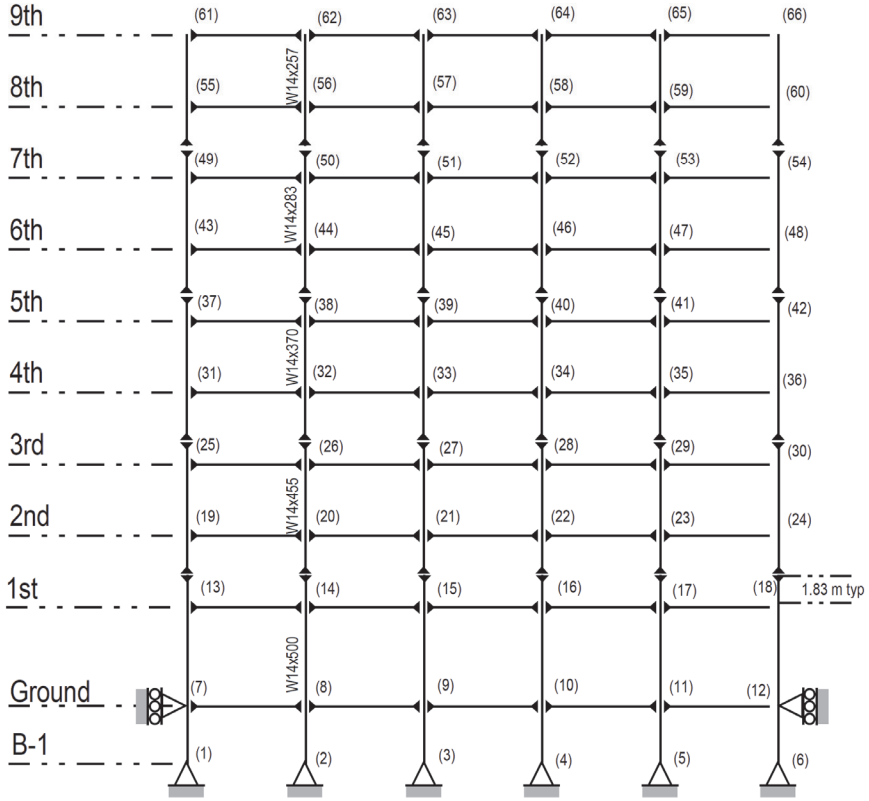

Figure 6.1: Elevation view of nine-story structure (Ohtori et al., 1994).

Structural control provided by MR dampers (added to the structure for this study) is assumed to keep response of the structure in the linear range for the earthquakes investigated. In this RTHS, the MR damper is represented by a physical specimen, while the rest of the structure is simulated numerically. The seismic mass that each NS moment frame must resist is 4.50×10^6 kg which is equivalent to 44,100 kN. A reasonable level of

control can be achieved with about 10% of this force, or 4410 kN. Because a 200 kN MR damper is available as the physical specimen, 18 of these devices are assumed to be used in conjunction with the moment frame to resist lateral loads. MR dampers with higher capacities have been developed, so it is possible to reduce the number of dampers in a physical implementation of this study. All 18 devices will be placed between the ground and the first story. By doing so, the need to test multiple devices is eliminated as the force from one MR damper can represent all 18.

The structure is assumed to be equipped with sensors measuring the absolute story accelerations in the first, third, fifth, seventh, and ninth floor, the MR damper displacement, and the MR damper force. These measurements are available to any semi-active controller for use in determining the input current to the MR damper. Two passive controllers are considered in addition to one semi-active controller. In the passive controllers, the input current is maintained at 0.0 or 2.5 Amps for passive-off and passive-on, respectively. The semi-active control is based on the clipped-optimal control algorithm (Dyke et al., 1996), i.e.,

$$i_{\mathrm{d}} = i_{\max} H\{(f_{\mathrm{d}} - f_{\mathrm{m}}) f_{\mathrm{m}}\} \tag{6.1}$$

Where i_{d} is the desired current (sent to MR damper), $i_{\max}$ is the maximum current (2.5 Amps in this case), f_{d} is the desired force, f_{m} is the measured force, and H is the Heaviside function. In short, when the desired force f_{d} is greater in magnitude than the measured force f_{m} and of the same sign, the maximum current $i_{\max}$ is sent to the damper. Thus, the magnitude of the force f_{m} will increase in an attempt to reach f_{d}. In all other cases, the current is set to 0.0 Amps.

The desired force f_{d} is determined using an LQG controller. The LQG controller was designed with equal acceleration weighting on all stories paired with very low weighting of the MR damper force. These weightings achieve good semi-active control results in simulation over wide range of earthquake records. More details applying semi-active control to large-scale MR dampers, including compensation techniques for the damper response lag, can be found in Friedman et al. (2010) and Phillips et al. (2010).

High-Fidelity MR Damper Model

To assist in developing semi-active control algorithms, a high-fidelity MR damper model is identified. This model can also be used to assess the effects of varying time delays, time lags, and amplitude dynamics. Of course, the results of such simulations are restricted by the accuracy of the model.

The MR damper was experimentally characterized using: (a) sine wave tests over a broad range of frequencies, amplitudes, and current levels, (b) triangle wave tests at a variety of velocities, (c) force rise time tests for step increases in current at constant velocities, and (d) force decay time tests for step decreases in current at constant velocities. This comprehensive characterization of the MR damper behavior was used to develop parameters for the phenomenological model originally proposed by Spencer et al. (1997) which is based on a Bouc-Wen hysteretic model. Other MR damper models have been proposed based on a Dahl friction model (Ikhouane and Dyke, 2007) and a hyperbolic tangent function (Kwok et al., 2006; Bass and Christenson, 2007; Jiang and Christenson, 2011). These models boast fewer parameters with comparable results to the

phenomenological model (Kwok et al., 2006; Ikouane and Dyke, 2007). A comprehensive evaluation of MR damper models can be found in Jiang and Christenson (2011). Little effort was required to fit the parameters of the phenomenological model to the 200 kN MR damper characterization tests, therefore this well-established model was employed without difficulty. Figure 6.2 illustrates the underlying mechanics of the model. Essentially the model outputs the restoring force F for a given input displacement x and velocity $\dot{x}$. Equating the forces on either side of the center rigid bar in Figure 6.2 leads to the following:

$$c_1\dot{y} = \alpha z + k_0(x - y) + c_0(\dot{x} - \dot{y}) \tag{6.2}$$

The force αz is determined by the evolutionary variable z modeled by the Bouc-Wen element.

$$\dot{z} = -\gamma|\dot{x} - \dot{y}|z|z|^{n-1} - \beta(\dot{x} - \dot{y})|z|^n + A(\dot{x} - \dot{y}) \tag{6.3}$$

The restoring force F can be described by equating the forces on either side of the right-hand-side rigid bar in Figure 6.2.

$$F = \alpha z + c_0(\dot{x} - \dot{y}) + k_0(x - y) + k_1(x - x_0) \tag{6.4}$$

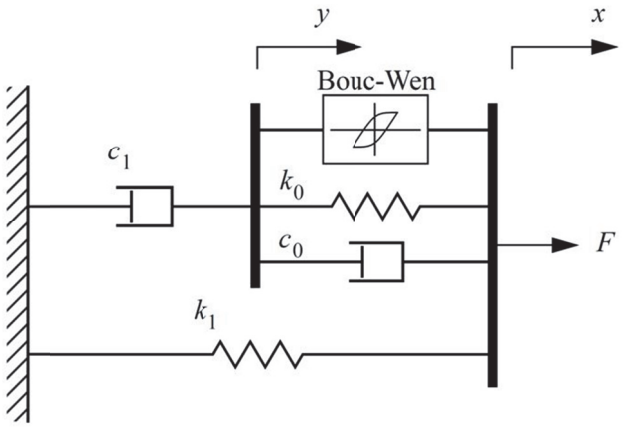

Figure 6.2: Phenomenological model of an MR damper.

Because the MR damper piston rod is double-ended, no force offset is present under zero displacement; thus, the stiffness term k_1 can be set to zero. The other model parameters are fit using Simulink's parameter estimation tool within MATLAB. To model the current dependent behavior of the MR damper, Equations (6.5) to (6.9) are incorporated into the model, where i_c is the input current. Parameters with the subscript a were fit to 0.0 Amp data while parameters with subscript b were fit to 2.5 Amp data. An exponential relationship between the extremes was found best to match the behavior intermediate levels of current, with the rate of change described by the parameters with subscript c. The optimized parameters are presented in Table 6.1.

$$\alpha = \alpha_{\mathrm{b}} + (\alpha_{\mathrm{a}} - \alpha_{\mathrm{b}})e^{(-\alpha_{\mathrm{c}} i_{\mathrm{c}})} \tag{6.5}$$

$$c_0 = c_{0,\mathrm{b}} + \left(c_{0,\mathrm{a}} - c_{0,\mathrm{b}}\right)e^{(-c_{0,\mathrm{c}} i_{\mathrm{c}})} \tag{6.6}$$

$$c_1 = c_{1,\mathrm{b}} + \left(c_{1,\mathrm{a}} - c_{1,\mathrm{b}}\right)e^{(-c_{1,i} i_{\mathrm{c}})} \tag{6.7}$$

$$\beta = \beta_{\mathrm{b}} + (\beta_{\mathrm{a}} - \beta_{\mathrm{b}})e^{(-\beta_{\mathrm{c}} i_{\mathrm{c}})} \tag{6.8}$$

$$\gamma = \gamma_{\mathrm{b}} + (\gamma_{\mathrm{a}} - \gamma_{\mathrm{b}})e^{(-\gamma_{\mathrm{c}} i_{\mathrm{c}})} \tag{6.9}$$

Table 6.1: Phenomenological model parameters for 200 kN MR damper.

Parameter	Value	Parameter	Value	Parameter	Value
$c_{0,\mathrm{a}}$	0.080 kN·sec/mm	$c_{1,\mathrm{a}}$	3.0 kN·sec/mm	$\gamma_{\mathrm{a}}, \beta_{\mathrm{a}}$	0.050 mm^{-2}
$c_{0,\mathrm{b}}$	0.32 kN·sec/mm	$c_{1,\mathrm{b}}$	15.0 kN·sec/mm	$\gamma_{\mathrm{b}}, \beta_{\mathrm{b}}$	0.0020 mm^{-2}
$c_{0,\mathrm{c}}$	1.5 A^{-1}	$c_{1,\mathrm{c}}$	2.0 kN·sec/mm	$\gamma_{\mathrm{c}}, \beta_{\mathrm{c}}$	5.2 A^{-1}
k_0	0.0 kN/mm	α_{a}	0.11 kN/mm	A	300
k_1	0.0 kN/mm	α_{b}	0.55 kN/mm	n	2.0
x_0	0.0 mm	α_{c}	1.0 A^{-1}		

Aside from the current dependent behavior of the MR damper at static levels of current, changes in current introduce dynamics that must be modeled. These dynamics can be described as a time lag consisting of two components: (a) the lag between when a current is commanded to the PWM device and it is realized in the MR damper circuit, and (b) the lag between when the current is realized in the MR damper circuit and the restoring force is achieved in the MR damper. The aggregate effects of both dynamics are modeled by a first order transfer function (Equation 6.10) curve fit to match experimentally collected force rise time data. The desired current i_{d} is input to the transfer functions and the effective resulting current i_{c} is then input to the MR damper model. Note that a second-order low pass filter with cutoff frequency of 75 Hz is added in series with Equation (6.10) to avoid model stability issues found for quickly changing current.

$$i_{\mathrm{c}} = \frac{(s+9\pi)}{9(s+\pi)} i_{\mathrm{d}} \tag{6.10}$$

To verify the proposed MR damper model under semi-active conditions (varying current), a BLWN with a 0−5 Hz bandwidth and a 2.78 mm RMS was input to the physical MR damper. At the same time, a current pulse between 0.0 and 2.5 Amps was input at a frequency of 2 Hz (50% duty cycle). The resulting displacement, velocity, and current histories from the experiment were then input into the numerical model. A comparison between the restoring force of the physical MR damper and model MR damper is presented in Figure 6.3. Force time histories, as well as force-displacement and force-velocity hysteresis loops, are shown. The model is seen to work well even under varying specimen conditions, although inaccuracies are apparent, especially after the current decreases. Differences between the model and physical specimen highlight the need for RTHS in that the highly nonlinear behavior of the MR damper cannot be completely captured by current modeling approaches.

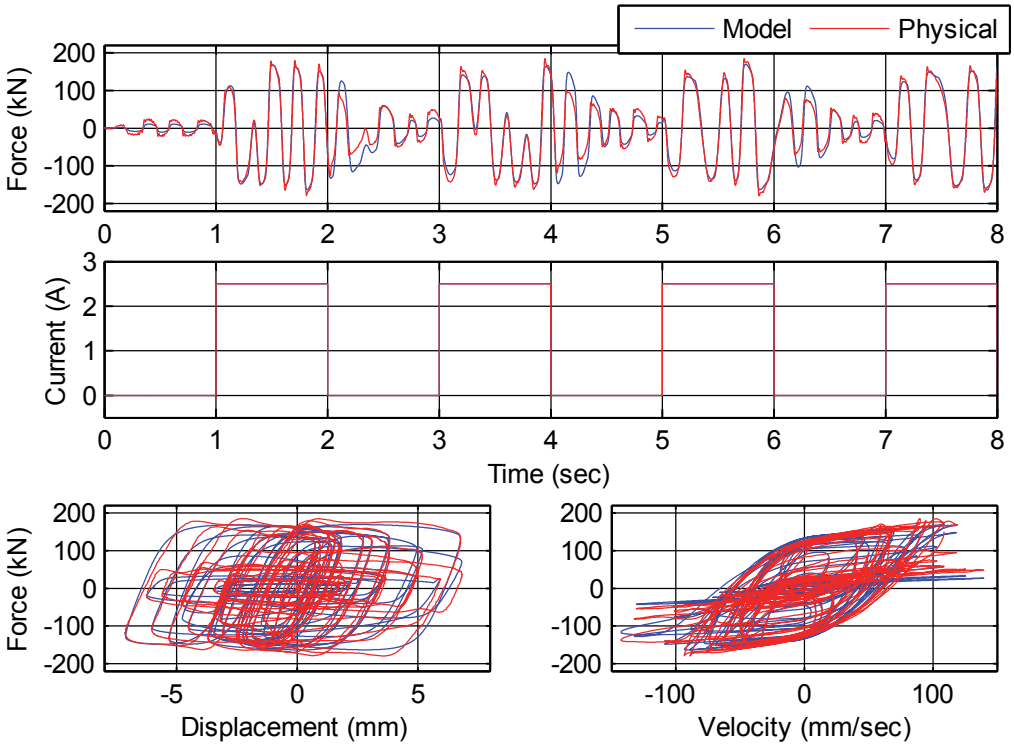

Figure 6.3: Performance of MR damper model under semi-active conditions.

BENCHMARK STRUCTURE
REAL-TIME HYBRID SIMULATION RESULTS

RTHS was used to evaluate the response of the nine-story structure subjected to the NS component of the 1940 El Centro earthquake with a scale factor of 0.5 (PGA 0.174 g). The numerical model, structural control algorithm, and real-time servo-hydraulic control techniques were implemented in Simulink. A sampling rate of 2000 Hz was found adequate at achieving both numerical integration accuracy (using the central difference method) and accuracy of the applied velocity to the MR damper.

Results from the RTHS are presented for the physical specimen in passive-off, passive-on and semi-active control modes in Figures 7.1 through 7.3. These figures show the time histories of the displacement and force of the MR damper, the ninth-story acceleration, as well as the force-displacement hysteresis and the force-velocity hysteresis of the MR damper. Numerical simulation results are also presented using the phenomenological model to represent the physical MR damper.

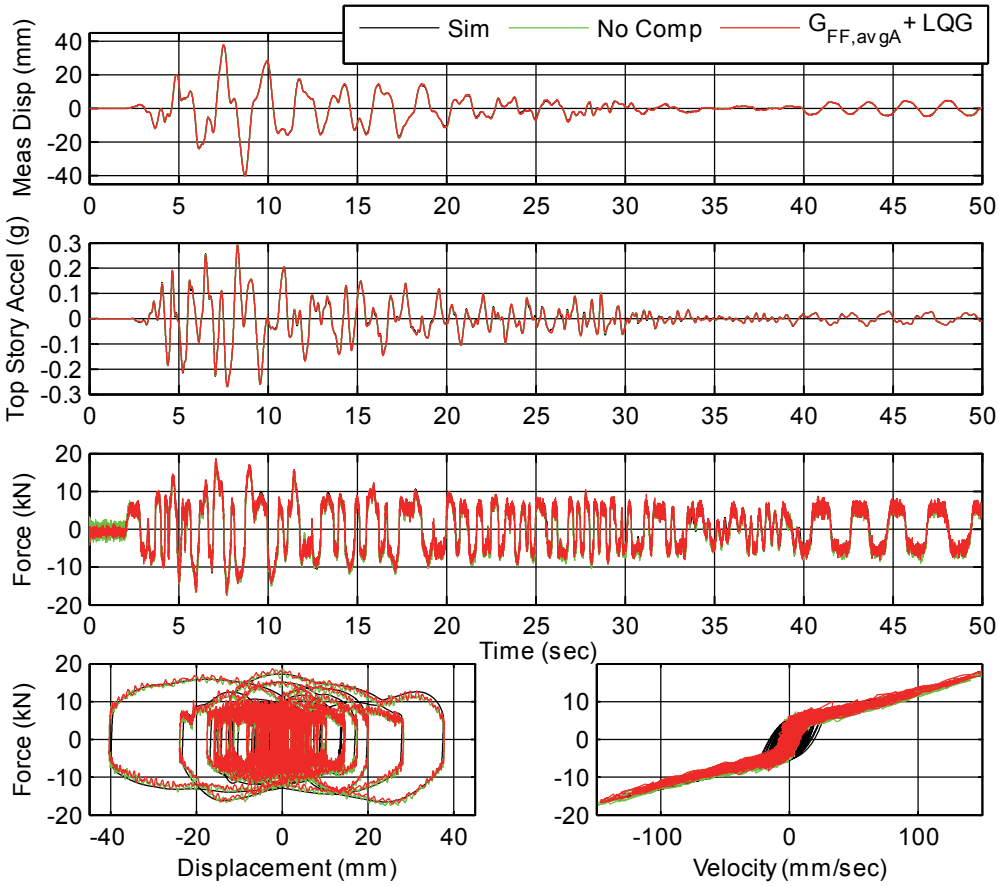

Figure 7.1: MR Damper response using passive-off control.

The proposed model-based servo-hydraulic tracking control strategy for this application (three pole transfer function models with the central difference method) requires an extrapolation of the acceleration followed by a prediction of velocity. The RMS errors between the extrapolated acceleration and the actual acceleration one time step later are 1.33%, 2.23%, and 1.81% for the passive-off, passive-on, and semi-active control modes presented below. The RMS errors between the predicted velocity and actual velocity one time step later are 0.0029%, 0.0119%, and 0.0061% for the passive-off, passive-on, and semi-active control modes presented below. The low RMS error indicates that the extrapolated and predicted values provide accurate estimates toward implementing an improper inverse.

The results for passive-off control are presented in Figure 7.1. While the RMS error is 3.05% without compensation and 0.381% with model-based feedforward-feedback tracking control, the two results from the RTHS are quite similar. This close agreement is due to the fact that in passive-off control, the restoring force returned to the numerical substructure is relatively small. Thus, even if the restoring force has some time lag, it has little influence on the overall structural response. Also, the MR damper naturally adds some damping to the system which can counteract the negative damping included by the time lag. Simulations match the RTHS well, indicating that the MR damper model is doing a good job capturing the MR damper nonlinearities and providing confidence in the results.

The results for passive-on control are presented in Figure 7.2. Unlike passive-off control, the RTHS could not be completed in the absence of compensation due to large, unsafe oscillations in the servo-hydraulic actuator. In lieu of uncompensated results, results using 3rd order polynomial extrapolation based on a 10 msec delay are presented. The force time history shows that for the polynomial extrapolation, some high-frequency oscillations are introduced because of the poor compensation provided at the higher frequencies. These oscillations are also present in the displacement time history, but much less apparent. Model-based feedforward-feedback tracking control exhibits excellent performance and does not introduce high-frequency oscillations. The RMS errors are 1.22% and 0.571% for polynomial extrapolation and model-based cases, respectively. The simulation matches the RTHS well, showing that the MR damper model also replicates the physical MR damper behavior for passive-on conditions.

Accurate real-time servo-hydraulic control is critical for passive-on control, which is counterintuitive, as passive-on control introduces more damping to the system than passive-off control. However, with the increase in damping also comes an increase in stiffness. At very small displacements (e.g. from 32 to 42 seconds in Figure 7.2) the MR damper behaves more like a spring, because the MR fluid is not yielding. Higher stiffness leads to more negative damping in the presence of time lag (Horiuchi et al., 1996). When the MR damper starts to move more significantly under the earthquake load, the additional damping provided by the MR damper helps to stabilize the oscillations. For the same reason, the oscillations do not grow without bound. The more the MR damper oscillates, the more positive damping is added to the system, stabilizing it. However, these oscillations can be damaging to the servo-hydraulic equipment. Also if the oscillations occur at a lightly damped mode or a mode significant to the structural response, the RTHS accuracy would be greatly reduced.

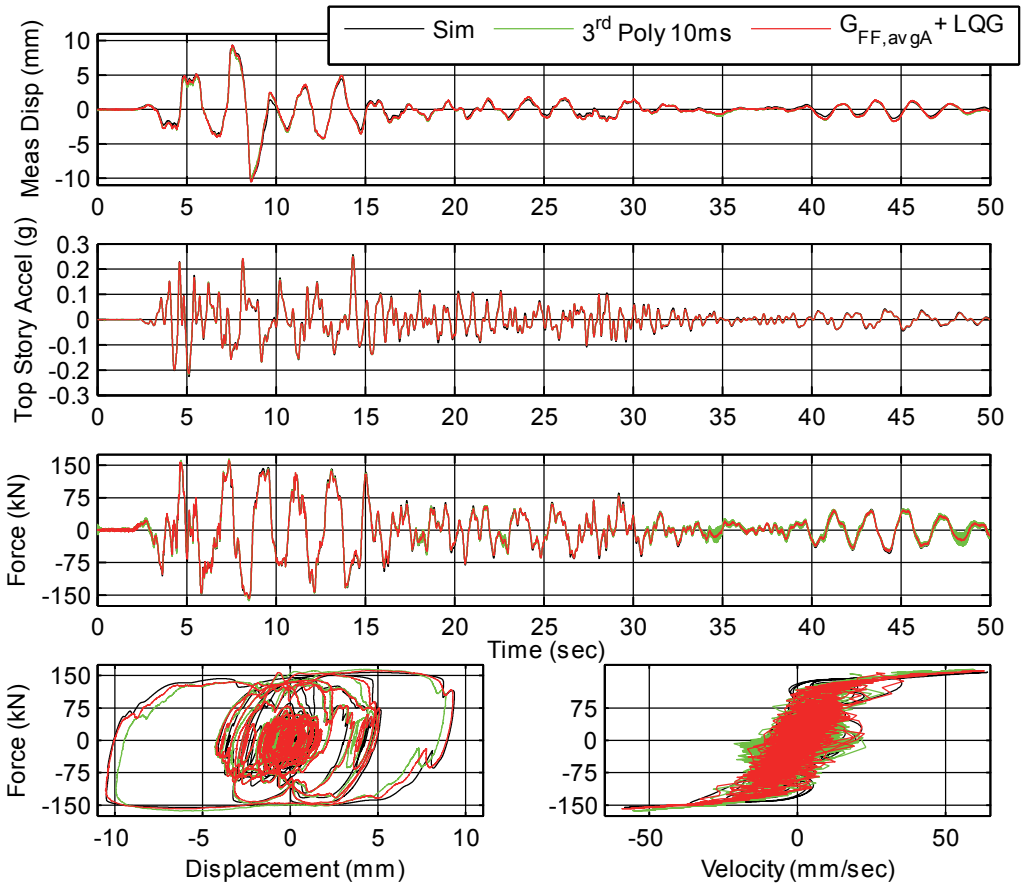

Figure 7.2: MR Damper response using passive-on control.

In the final structural controller explored, the MR damper current was allowed to vary using the semi-active clipped-optimal control scheme, with results presented in Figure 7.3. As with the passive-on case, the RTHS quickly became unstable in the absence of compensation.

Semi-active control switches the specimen conditions between the extremes very quickly, adding high-frequency dynamics to the structure. The 3rd order polynomial extrapolation technique handles these additional dynamics poorly, leading toward high amplitude oscillations in the force, most apparent in the hysteresis. On the other hand, results are similar for both the model-based bumpless transfer controller and proposed model-based feedforward-feedback tracking controller. Small oscillations in the force are apparent with the bumpless transfer controller, which are likely due to the low-pass filter adding phase lag to the controller at these frequencies. The RMS errors are 0.667%, 0.302% and 0.379% for the 3rd order polynomial extrapolation, bumpless transfer, and feedforward-feedback control, respectively.

As with the other structural control cases (passive-off and passive-on), the numerical simulation matches the RTHS well. The differences can be attributed to the difficulty in modeling the behavior of the MR damper under changing current, as well as the semi-active control affecting future control efforts. These challenges aside, the model provides

a good comparison even for the semi-active case and more importantly, a useful tool for semi-active controller design.

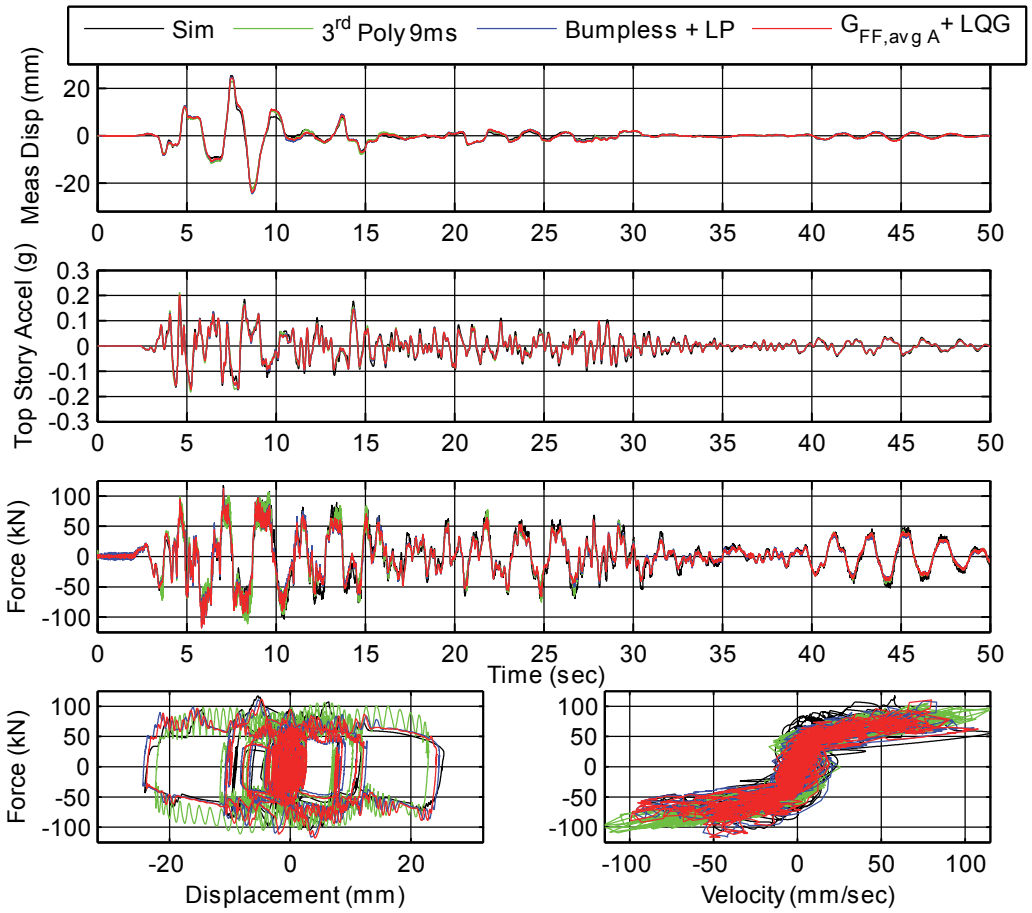

Figure 7.3: MR Damper response using clipped-optimal control.

In regard to the performance of the MR damper as a semi-active device, a reduction in top story acceleration is seen when compared to the passive-on case. The maximum acceleration drops from 0.250 g's to 0.203 g's while the RMS acceleration drops from 0.0520 g's to 0.0425 g's. At the same time, the maximum control force decreases from 162 kN to 118 kN. Semi-active control is seen to be an effective a means to balance between good displacement and acceleration performance under a wide range of input loads. A complete study of semi-active control strategies for this structure is outside of the scope of this report.

The RTHS conducted for this report was an especially challenging case for real-time servo-hydraulic control. This difficulty arises from the fact that the building is lightly damped at high frequencies and the central difference method adds no numerical damping. Light damping brings the structure closer to instability when coupled inadequately compensated time delay and time lag. At the same time, a single physical MR damper is used to represent 18 devices. Any measurement noise in the dampers is amplified and completely correlated. Also, the harmful effects of time delay and time lag,

such as negative damping, are concentrated in one location and amplified. In spite of these challenges, model-based servo-hydraulic tracking control provided excellent results in RTHS.

Also, note that the displacement, velocity, and acceleration responses of the overall structure do not change much with the compensation methods explored. The most significant effects are local to the MR damper, namely stability of the physical experiment and undesired oscillations at floors connected to the MR damper. However, these higher frequency oscillations are not significant to the overall response of the structure (in this case) and do not travel far from the source. It is worth mentioning that if the MR damper placement were different, the load cell measurement noise and any destabilizing negative damping would enter different stories of the structure and thus affect difference frequencies of vibration.

CONCLUSION

This report provides a rigorous framework for model-based servo-hydraulic tracking control including both model-based feedforward and feedback links to directly address added, unwanted dynamics in the RTHS loop. A simple approach to developing a model-based servo-hydraulic tracking controller for a general servo-hydraulic system has been proposed. With predefined displacements, results showed near perfect tracking of the desired displacement signal. In RTHS, the proposed model-based controller was proven successful for testing SDOF structures in a parametric study and a lightly damped MDOF structure, both using a 200 kN MR damper as the physical substructure. In the SDOF test, the proposed model-based controller provided the best tracking among the methods considered, especially when the natural frequency of the structure exceeded 5 Hz. In the MDOF test, the current in the MR damper was allowed to vary under semi-active control. Even under these changing specimen conditions which introduce higher frequency dynamics into the RTHS, the proposed model-based controller showed excellent performance. For the numerical simulations, a phenomenological model is proposed to accurately represent the 200 kN MR damper dynamics under semi-active conditions. Numerical simulation results compared well to RTHS, proving confidence in RTHS results.

REFERENCES

Ahmadizadeh A, G Mosqueda, and AM Reinhorn. (2008). "Compensation of actuator dynamics for real-time hybrid simulation." *Earthquake Engineering and Structural Dynamics* 2008. 37(1): 21-42.

Bass BJ and RE Christenson. (2007). "System Identification of a 200 kN Magneto-Rheological Fluid Damper for Structural Control in Large-Scale Smart Structures." *Proceedings of the 2007 American Control Conference*, New York, USA, Paper No. ThA17.6. 2690-2695.

Carrion JE and BF Spencer Jr. (2007). "Model-based strategies for real-time hybrid testing." *Newmark Structural Engineering Laboratory Report Series*, University of Illinois at Urbana-Champaign, Urbana, IL, No. 6.

Carrion JE, BF Spencer Jr., and BM Phillips. (2009). "Real-Time Hybrid Simulation for Structural Control Performance Assessment." *Earthquake Engineering and Engineering Vibration*, 8(4): 481-492.

Chen C and JM Ricles. (2010). "Tracking Error-Based Servohydraulic Actuator Adaptive Compensation for Real-Time Hybrid Simulation." *Journal of Structural Engineering*, 136(4): 432-440.

Christensen RE, Y Lin, A Emmons, and B Bass. (2008). "Large-Scale Experimental Verification of Semi-Active Control through Real-Time Hybrid Simulation." *Journal of Structural Engineering*. 134(4): 522-534.

Darby AP, A Blakeborough, and MS Williams. (1999). "Real-time substructure tests using hydraulic actuator." *Journal of Engineering Mechanics*, 125(10): 1133-1139.

Darby AP, A Blakeborough, and MS Williams. (2001). "Improved control algorithm for real-time substructure testing." *Earthquake Engineering and Structural Dynamics*, 30(3): 431–448.

Darby AP, MS Williams, and A Blakeborough. (2002). "Stability and delay compensation for real-time substructure testing." *Journal of Engineering Mechanics*, 128(12): 1276-1284.

Dyke SJ, BF Spencer Jr., MK Sain, and J. D. Carlson. (1996). "Modeling and Control of Magnetorheological Dampers for Seismic Response Reduction." *Smart Materials and Structures*, 5(5): 565-575.

Dyke SJ, BF Spencer Jr., P Quast, and MK Sain. (1995). "Role of control-structure interaction in protective system design." *Journal of Engineering Mechanics*, 121(2): 322-338.

Friedman, AJ, J Zhang, BM Phillips, Z Jiang, A Agrawal, JM Ricles, BF Spencer Jr., R Sause, and RE Christenson. (2010). "Accomodating MR damper Dynamics for Control of Large Scale Structural Systems." *Proceedings of the Fifth World Conference on Structural Control and Monitoring*, Shinjuku, Tokyo.

Horiuchi T, M Inoue, T Konno, and Y Namita. (1999). "Real-time hybrid experimental system with actuator delay compensation and its application to a piping system with energy absorber." *Earthquake Engineering and Structural Dynamics*, 28(10): 1121-1141.

Horiuchi T, M Nakagawa, M Sugano, and T Konno. (1996). "Development of a real-time hybrid experimental system with actuator delay compensation." *Proceedings of the 11th World Conf. Earthquake Engineering*, Paper No. 660.

Horiuchi T, and T Konno. (2001). "A New Method for Compensating Actuator Delay in Real-Time Hybrid Experiments." *Philosophical Transaction of the Royal Society: Theme Issue on Dynamic Testing of Structures*. A359: 1893-1909.

Ikhouane F and SJ Dyke. (2007). "Modeling and Identification of a Shear Mode Magnetorheological Damper." *Smart Materials and Structures*, 16(3): 605-616.

Jiang Z and RE Christenson. (2010). "A Comparison of 200 kN magneto-rheological damper models for use in real-time hybrid simulation pretesting." *Smart Materials and Structures*, 20(6).

Jung RY, PB Shing, E Stauffer, and B Thoen. (2007). "Performance of a real-time pseudodynamic test system considering nonlinear structural response." *Earthquake Engineering and Structural Dynamics*, 36(12):1785-1809.

Kwok NM, QP Ha, TH Nguyen, J Li, and B Samali. (2006). "A Novel Hysteretic Model for Magnetorheological Fluid Dampers and Parameter Identification using Particle Swarm Optimization." *Sensors and Actuators A: Physical*, Elsevier, 132(2): 441-451.

Lewis FL and VL Syrmos. (1995). *Optimal Control*. Second Edition. Wiley-Interscience, John Wiley & Sons, Inc., New York, pp. 377-393.

Nakashima M, H Kato, and E Takaoka. (1992). "Development of real-time pseudo dynamic testing." *Earthquake Engineering and Structural Dynamics*, 21(1): 79-92.

Nakashima M and N Masaoka. (1999). "Real time on-line test for MDOF systems." *Earthquake Engineering and Structural Dynamics*, 28(4): 393-420.

Ohtori Y, RE Christenson, and BF Spencer Jr. (1994). "Benchmark Control Problems for Seismically Excited Nonlinear Buildings." *Journal of Engineering Mechanics*, 130(4): 366-385.

Phillips BM, Y Chae, Z Jiang, BF Spencer Jr., JM Ricles, RE Christenson, SJ Dyke, and A Agrawal. (2010). "Real-Time Hybrid Simulation Benchmark Structure with a Large-Scale MR Damper." *Proceedings of the Fifth World Conference on Structural Control and Monitoring*, Shinjuku, Tokyo.

Shing PB, Z Wei, RY Jung, E Stauffer. (2004). "NEES fast hybrid test system at the University of Colorado." *Proceedings of the 13th World Conference on Earthquake Engineering*, Vancouver, Canada, Paper No. 3497.

Soong TT and BF Spencer Jr. (2002). "Supplemental energy dissipation: state-of-the-art and state-of-the-practice." *Engineering Structures*, 24: 243-259.

Spencer BF, Dyke SJ, Sain MK, and Carlson JD. (1997). "Phenomenological Model for Magnetorheological Dampers." *Journal of Engineering Mechanics*, 123(3): 230-238.

Stengel RF. (1986). *Stochastic Optimal Control: Theory and Application*. John Wiley & Sons, New York.

Wallace M, DJ Wagg, and SA Neild. (2005). "An Adaptive Polynomial Based Forward Prediction Algorithm for Multi-Actuator Real-Time Dynamic Substructuring." *Proceedings of the Royal Society*, A461: 3807-3826.

Wallace MI, DJ Wagg, SA Neild, P Bunnis, NAJ Lieven AJ Crewe. (2007). "Testing coupled rotor blade-lag damper vibration using real-time dynamic substructuring." *Journal of Sound and Vibration*, 307(3-5): 737-754.

Wu B, H Bao, J Ou, and S Tian. (2005). "Stability and accuracy ansysis of the central difference method for real-time substructure testing." *Earthquake Engineering and Structural Dynamics*, 34(14): 705-718.

Yang G, BF Spencer Jr., JD Carlson, and MK Sain. (2002). "Large-Scale MR Fluid Dampers: Modeling and Dynamic Performance Considerations." *Engineering Structures*, 24(3): 309-323.

List of Recent NSEL Reports

No.	*Authors*	*Title*	*Date*
013	Pallarés, L. and Hajjar, J.F.	Headed Steel Stud Anchors in Composite Structures: Part I – Shear	April 2009
014	Pallarés, L. and Hajjar, J.F.	Headed Steel Stud Anchors in Composite Structures: Part II – Tension and Interaction	April 2009
015	Walsh, S. and Hajjar, J.F.	Data Processing of Laser Scans Towards Applications in Structural Engineering	June 2009
016	Reneckis, D. and LaFave, J.M.	Seismic Performance of Anchored Brick Veneer	Aug. 2009
017	Borello, D.J., Denavit, M.D., and Hajjar, J.F.	Behavior of Bolted Steel Slip-critical Connections with Fillers	Aug. 2009
018	Rice, J.A. and Spencer, B.F.	Flexible Smart Sensor Framework for Autonomous Full-scale Structural Health Monitoring	Aug. 2009
019	Sim, S.-H. and Spencer, B.F.	Decentralized Strategies for Monitoring Structures using Wireless Smart Sensor Networks	Nov. 2009
020	Kim, J. and LaFave, J.M.	Joint Shear Behavior of Reinforced Concrete Beam-Column Connections subjected to Seismic Lateral Loading	Nov. 2009
021	Linderman, L.E., Rice, J.A., Barot, S., Spencer, B.F., and Bernhard, J.T.	Characterization of Wireless Smart Sensor Performance	Feb. 2010
.			
022	Miller, T.I. and Spencer, B.F.	Solar Energy Harvesting and Software Enhancements for Autonomous Wireless Smart Sensor Networks	March 2010
023	Denavit, M.D. and Hajjar, J.F.	Nonlinear Seismic Analysis of Circular Concrete-Filled Steel Tube Members and Frames	March 2010
024	Spencer, B.F. and Yun, C.-B. (Eds.)	Wireless Sensor Advances and Applications for Civil Infrastructure Monitoring	June 2010
025	Eatherton, M.R.. and Hajjar, J.F.	Large-Scale Cyclic and Hybrid Simulation Testing and Development of a Controlled-Rocking Steel Building System with Replaceable Fuses	Sept. 2010
026	Hall, K., Eatherton, M.R., and Hajjar, J.F.	Nonlinear Behavior of Controlled Rocking Steel-Framed Building Systems with Replaceable Energy Dissipating Fuses	Oct. 2010
027	Yeo, D. and Jones, N.P.	Computational Study on 3-D Aerodynamic Characteristics of Flow around a Yawed, Inclined, Circular Cylinder	Mar. 2011
028	Phillips, B.M. and Spencer, B.F.	Model-Based Feedforward-Feedback Tracking Control for Real-Time Hybrid Simulation	Aug. 2011